Journal of Constructional Steel Research 227 (2025) 109332

Contents lists available at ScienceDirect

Journal of Constructional Steel Research

journal homepage: www.elsevier.com/locate/jcsr

Tensile stress-strain models for wire and arc additive manufacturing of carbon steels

Yunyi Liu [a], Jun Ye [b,*], Xi Guo [c], Guan Quan [a], Zhen Wang [d], Yang Zhao [e]

[a] College of Civil Engineering and Architecture, Zhejiang University, Hangzhou 310058, China
[b] School of Civil Engineering, University of Leeds, Leeds LS2 9JT, UK
[c] Department of Civil and Environmental Engineering, Imperial College London, London SW7 2AZ, UK
[d] Department of Civil Engineering, Hangzhou City University, Hangzhou 310015, China
[e] School of Civil Engineering, Shaoxing University, Shaoxing, China

ARTICLE INFO

Keywords:
Metal 3D printing
Wire and arc additive manufacturing
Carbon steel
Stress-strain models

ABSTRACT

This paper aims to investigate and develop stress-strain models for wire arc additive manufacturing (WAAM) carbon steels, providing a clear understanding of their mechanical behaviour. A comprehensive dataset comprising over 700 worldwide WAAM carbon steel tensile coupon test records from open literature was analysed. The dataset considered a variety of feedstock wires, post-treatments, surface conditions, deposition strategies, coupon extraction angles, and material thicknesses. Analysis revealed that stress-strain curves of WAAM carbon steels exhibited varying yielding responses, either discontinuous yielding with a distinct yield plateau or continuous yielding without one, depending on the feedstock wire grades and coupon extraction angles. Three tensile stress-strain models were proposed, alongside predictive expressions or recommended values for the input material parameters. These models accurately capture the stress-strain responses of WAAM carbon steels and are suitable for incorporation into analytical, numerical and design models for WAAM steel structures.

1. Introduction

Amidst the flourishing additive manufacturing (AM) industry, Wire Arc Additive Manufacturing (WAAM) establishes a foothold for its combination of traditional welding techniques with advanced robotics to enable layer-by-layer structure fabrication, as shown in Fig. 1.

WAAM is exceptionally well-suited for application in the construction industry for its friendliness towards producing large-scale and intricately optimised structures, in addition to the fast production speed and high material utilisation [1–4]. The WAAM technology has been effectively employed in fabricating the cantilever truss [4,5], beam hook [6], and footbridge [3,7], as depicted in Fig. 2.

This technology is applicable to a series of metal alloys, including stainless steel, carbon steel, aluminium, and titanium alloys, each offering unique properties customizable to specific application requirements. In recent years, research on the behaviours of WAAM metal materials has surged in material and construction field, mainly encompassing studies on stainless steel [8–11] and carbon steel [12–14]. These investigations have explored the effects of printing parameters, deposition strategies, post-treatments on the microstructure characteristics and mechanical properties of WAAM materials, providing valuable insights for optimising the printing process and improving the practical performance of printed structures [8,9,12–18]. Building on these findings, further research has focused on WAAM components such as columns [19–21] and bolted connections [22–27].

Various simplified models have been proposed to represent the material response of hot-rolled carbon steels, among which the linear models can be grouped as (1) elastic, perfectly-plastic, (2) elastic, linear hardening and (3) tri-linear [28]. These models are applicable to the case of simply ignore of strain hardening, no obvious yield plateau and simple neglect of strain hardening behaviour with gradual loss of stiffness. To accurately represent the elastic, yield plateau and strain hardening regimes, Yun and Gardner [28] proposed a quad-linear material model and a bilinear plus nonlinear hardening material model.

The Ramberg-Osgood model [29,30] is widely used to describe the rounded stress-strain response of metallic materials such as stainless steels, aluminium and cold-formed carbon steels that have undergone sufficient plastic deformation to eliminate the yield plateau. In studies on stainless steel, the basic Ramberg-Osgood model can accurately represent different regions of the stress-strain curve using different

* Corresponding author.
E-mail address: J.Ye2@leeds.ac.uk (J. Ye).

https://doi.org/10.1016/j.jcsr.2025.109332
Received 15 October 2024; Received in revised form 19 December 2024; Accepted 3 January 2025
Available online 13 January 2025

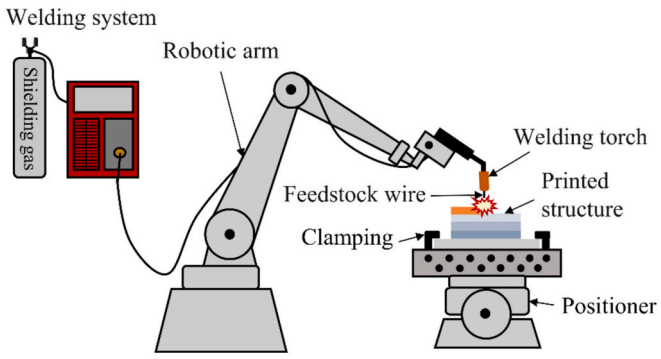

Fig. 1. Manufacturing equipment and printed structure of WAAM process.

values of the strain hardening exponent. However, a single strain hardening exponent value is insufficient to capture the full stress-strain curve. Therefore, improved two-stage models, three-stage models, and multistage models have been proposed successively [31–34]. For key material parameters, different grades of stainless steel require different predictive expressions [35]. Similar behaviours have also been observed in studies on cold-formed carbon steel [36]. Shi [37] suggested that the stress-strain curves of high-strength steels (HSSs) can be classified into two basic types: those exhibiting discontinuous yielding (with a distinct yield plateau) and those exhibiting continuous yielding (without a yield plateau). For the continuous yielding case, a revised multi-linear constitutive model was further proposed based on the typical Ramberg-Osgood model. Through the analysis of collected experimental data on HSSs, Wang [38] defined a criterion to determine the occurrence of the yield plateau according to the yield strength of the steel and its carbon content of the steels, and developed two stress-strain models for continuous and discontinuous yielding, respectively. However, for WAAM carbon steels, Huang [39] categorised the stress-strain models according to the yield strength into WAAM normal-strength steel and high-strength steel models, which were modified from quad-linear and bilinear plus nonlinear hardening material models, and a two-stage Ramberg-Osgood model, respectively.

Based on the analysis of the author's previous experiments and available research, it can be concluded that WAAM carbon steels typically exhibit stress-strain behaviour similar to that of conventionally produced steels, displaying both discontinuous and continuous yielding regardless of any yield strength. Differently, the geometric undulations in as-built WAAM components lead to a reduction in effective mechanical properties and introduce a certain degree of anisotropy. Therefore, accurately describing these characteristics and establishing a universal stress-strain response of WAAM carbon steel is an urgent problem to be solved, which is crucial for subsequent theoretical research, numerical analysis, and practical applications.

This paper aims to provide the predictive expressions or recommended values of the key material parameters required in the stress-strain models. This is based on the analysis of over 700 tensile coupon test records of WAAM carbon steel collected from global literature using Ordinary Least Squares (OLS) regression analysis. Possible interfering factors of stress-strain responses consist of a series of feedstock wires, post-treatments, surface conditions, deposition strategies, coupon extraction angles, and material thicknesses are considered. Additionally, drawing on existing stress-strain models applicable to conventionally produced steels, three stress-strain models exhibiting discontinuous yielding and continuous yielding are proposed for WAAM carbon steels. Finally, the predicted stress-strain curves are compared with the corresponding experimental curves, and the proposed models are used to simulate WAAM carbon steel coupons to evaluate the accuracy of the proposed models and applicability in structural analysis.

2. Existing stress-strain models

2.1. Models for conventionally produced steels

2.1.1. Models exhibiting discontinuous yielding

The typical stress-strain curve exhibiting discontinuous yielding of carbon steel (mainly hot-rolled carbon steels) is shown in Fig. 3. In the elastic range, the curve remains linear with a slope defined by the

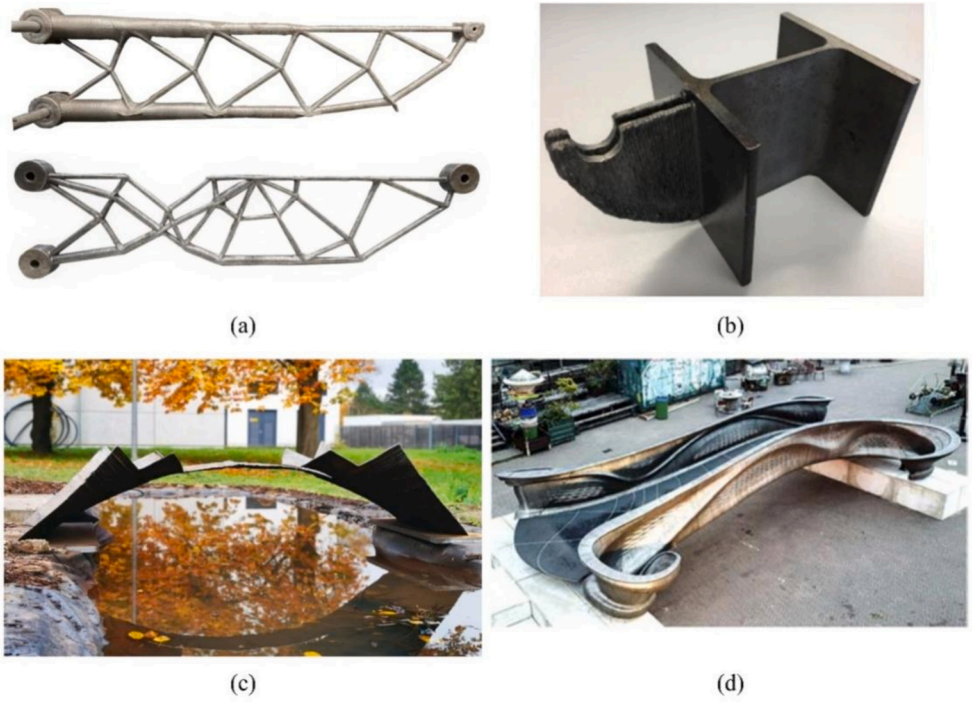

Fig. 2. WAAM structures: (a) a cantilever truss [4], (b) a beam hook [6], (c) a small 3D printed footbridge in shell form [7], and (d) a MX3D metal 3D printed footbridge [3].

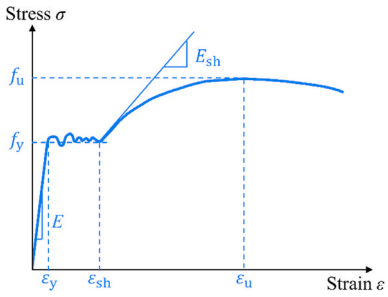

Fig. 3. Typical stress-strain curve of carbon steel with discontinuous yielding.

Young's modulus E. After entering the elastic-plastic range, the strain of the curve increases sharply while the stress fluctuates slightly within the upper and lower yield strengths. The lower yield strength is chosen as the yield strength f_y [40] in this paper and the yield strain ε_y can be calculated from f_y/E. When the strain reaches the strain hardening strain ε_{sh}, the strain hardening initiates. The stress increases again up to the ultimate stress f_u with a reduced rate defined as strain hardening modulus E_{sh}. The strain corresponds to f_u is defined as ultimate strain ε_u.

As summarised in the aforementioned section, various simplified models have been proposed to represent the stress-strain response of hot-rolled carbon steels, such as elastic, perfectly plastic model; elastic, linear hardening model; and tri-linear model as illustrated in Fig. 4(a), 4(b) and 4(c) respectively. Compared with the typical stress-strain curve in Fig. 3, the three models have their respective limitations, such as ignoring strain hardening, overlooking the distinct yield plateau, and neglecting the gradual loss of stiffness during the strain hardening behaviour.

Therefore, a quad-linear model and a bilinear plus nonlinear hardening model have been developed to address the limitations, as illustrated in Fig. 5 [28]. The quad-linear stress-strain model consists of four stages is written as Eq. (1).

$$f(\varepsilon)=\begin{cases} E\varepsilon & \text{for } \varepsilon \le \varepsilon_y \\ f_y & \text{for } \varepsilon_y < \varepsilon \le \varepsilon_{sh} \\ f_y + E_{sh}(\varepsilon-\varepsilon_{sh}) & \text{for } \varepsilon_{sh} < \varepsilon \le C_1\varepsilon_u \\ f_{C_1\varepsilon_u} + \dfrac{f_u - f_{C_1\varepsilon_u}}{\varepsilon_u - C_1\varepsilon_u}(\varepsilon - C_1\varepsilon_u) & \text{for } C_1\varepsilon_u < \varepsilon \le \varepsilon_u \end{cases} \tag{1}$$

where the $C_1\varepsilon_u$ represents the strain at the intersection point of the simplified initial strain hardening curve (i.e. the third stage of the model) and the actual stress-strain curve, and $f_{C_1\varepsilon_u}$ is the corresponding stress. The strain hardening modulus E_{sh} and the strain hardening strain ε_{sh} are calculated using Eq.(2) and Eq. (3), respectively [28].

$$E_{sh}=\frac{f_u - f_y}{C_2\varepsilon_u - \varepsilon_{sh}} \tag{2}$$

$$\varepsilon_{sh}=0.1\frac{f_y}{f_u}-0.055 \quad \text{for } 0.015 \le \varepsilon_{sh} \le 0.03 \tag{3}$$

Meanwhile, the bi-linear plus nonlinear hardening model shown in Fig. 5(b) and Eq. (4) was also proposed [28], which captures the gradual loss of stiffness in the strain hardening region thus is more suitable for advanced numerical simulations. Considering its practicality, the quad-linear model is deemed appropriate and sufficiently accurate for most engineering application.

$$f(\varepsilon)=\begin{cases} E\varepsilon & \text{for } \varepsilon \le \varepsilon_y \\ f_y & \text{for } \varepsilon_y < \varepsilon \le \varepsilon_{sh} \\ f_y + \left(f_u - f_y\right) \times \left\{ K_1\left(\dfrac{\varepsilon-\varepsilon_{sh}}{\varepsilon_u-\varepsilon_{sh}}\right) + K_2\left(\dfrac{\varepsilon-\varepsilon_{sh}}{\varepsilon_u-\varepsilon_{sh}}\right) \Big/ \left[1 + K_3\left(\dfrac{\varepsilon-\varepsilon_{sh}}{\varepsilon_u-\varepsilon_{sh}}\right)^{K_4}\right]^{\frac{1}{K_4}} \right\} & \text{for } \varepsilon_{sh} < \varepsilon \le \varepsilon_u \end{cases} \tag{4}$$

The material coefficients of strain hardening stage, C_1 and C_2 in Eq. (1), as well as K_1, K_2, K_3, and K_4 in Eq. (4), are calibrated using Ordinary Least Squares (OLS) regression analysis based on actual stress-strain curves beyond the strain hardening ε_{sh}. The measured stress-strain curves often contain unevenly distributed data points due to the varying strain rates during coupon testing, and in some cases, exhibit a high degree of experimental noise. These factors can cause problems for the OLS regression analysis. Therefore, before performing the regression analysis, the strain-hardening region of the original stress-strain curve is typically fitted to a 7th-order polynomial [41], as given by Eq. (5), where a_1 through a_7 represent a set of trial coefficients to be determined.

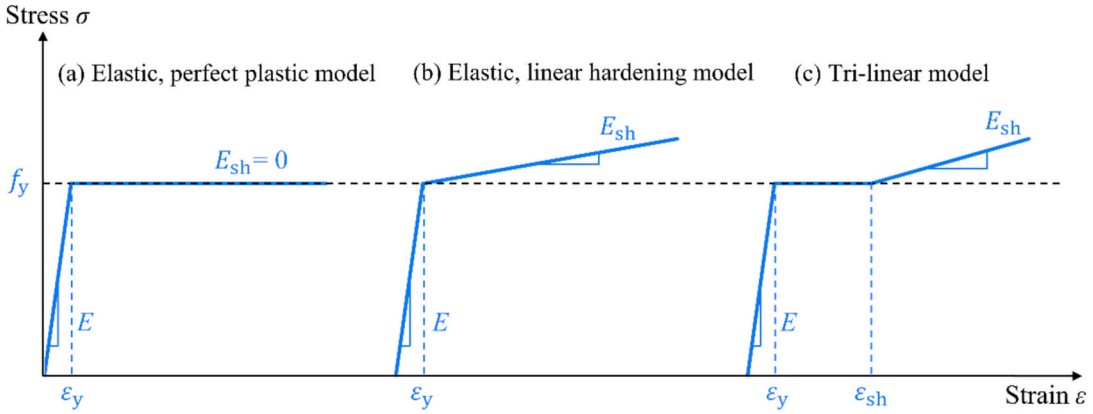

Fig. 4. Existing linear stress-strain models for hot-rolled carbon steels.

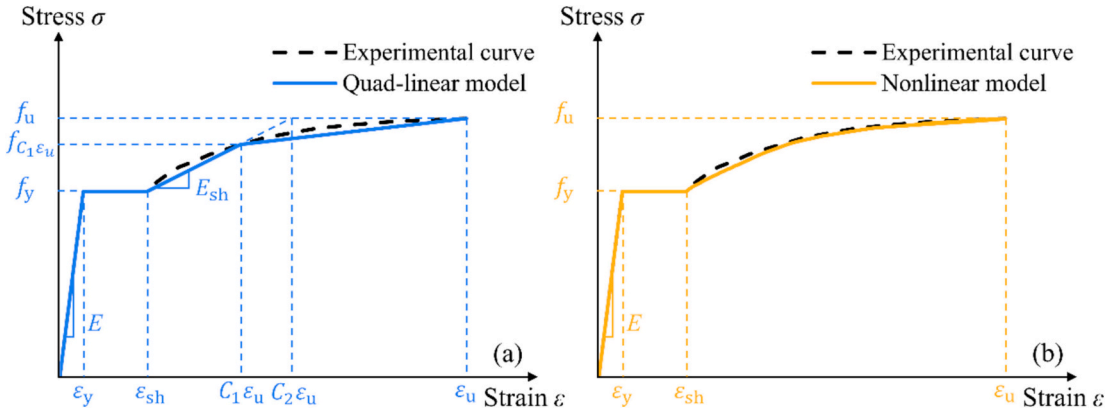

Fig. 5. Existing quad-linear and bilinear plus nonlinear hardening models: (a) quad-linear model with flat yield plateau; (b) bilinear plus nonlinear hardening model with flat yield plateau.

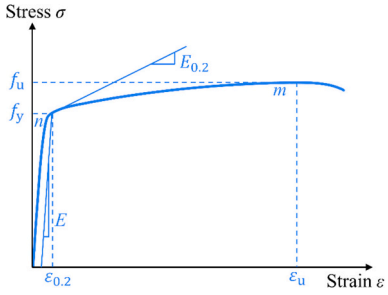

Fig. 6. Typical stress-strain curve of carbon steel with continuous yielding.

The material coefficients are then obtained based on the evenly distributed data points obtained from Eq. (5).

$$f(\varepsilon) = f_y + \sum_{k=1}^{7} a_k(\varepsilon - \varepsilon_{sh})^k \quad \text{for } \varepsilon_{sh} < \varepsilon \le \varepsilon_u \tag{5}$$

2.1.2. Models exhibiting continuous yielding

Fig. 6 illustrates the typical stress-strain curve with continuous yielding, which is mainly observed in stainless steels and cold-formed carbon steels. This behaviour is originally described by the basic Ramberg-Osgood model [29,30] by using three key material parameters, including the Young's modulus E, the yield strength f_y , and the strain hardening exponent n – see Eq. (6).

$$\varepsilon = \frac{f}{E} + 0.002\left(\frac{f}{f_y}\right)^n \tag{6}$$

Due to the rounded nature of the stress-strain curve, the 0.2 % proof stress $f_{0.2}$ is taken as the yield strength f_y. However, several equations have been proposed to calculate the strain hardening exponential n. The equation proposed by Hill [30] is given by Eq. (7) where f_1 and f_2 correspond to the 0.1 % and 0.2 % proof stress respectively, and ε_1 and ε_2 correspond the respective strain. The equation provided the fundamental form while 0.2 % proof stress f_y and 0.01 % proof stress $f_{0.01}$ are used in [32,33,42,43], and 0.2 % proof stress f_y and 0.05 % proof stress $f_{0.05}$ are used in [31,35,44], as shown in Eq. (8) and Eq. (9), respectively. In addition, EN 1993-1-4 [43] also provides a recommended value of n for convenience.

$$n = \frac{ln\left(\frac{\varepsilon_2}{\varepsilon_1}\right)}{ln\left(\frac{f_2}{f_1}\right)} \tag{7}$$

$$n = \frac{ln(20)}{ln\left(\frac{f_y}{f_{0.01}}\right)} \tag{8}$$

$$n = \frac{ln(4)}{ln\left(\frac{f_y}{f_{0.05}}\right)} \tag{9}$$

As noted in the preceding section, the use of the Ramberg-Osgood model [29,30] for stresses higher than f_y can lead to overestimation of stresses. To address this limitation, various multistage Ramberg-Osgood models have been developed. Fig. 6 illustrates the two-stage Ramberg-Osgood model [31], given by Eq. (10), and highlights the definitions of key material parameters associated with it. For the second stage ($f > f_y$), the new equation is derived by shifting both the vertical and horizontal axes from the origin to the point on the stress-strain curve corresponding to the 0.2 % proof stress f_y, then applying the Ramberg-Osgood model in this new reference system. For simplicity, or when the material demonstrates good ductility, the term $\varepsilon_{0.2} - \frac{f_u - f_y}{E_{0.2}}$ is selectively omitted, and a simplified model [32] is employed as Eq. (11). The initial modulus $E_{0.2}$ is the tangent modulus of the stress-strain curve at the 0.2 % proof stress, as obtained from Eq. (12).

$$\varepsilon = \begin{cases} \dfrac{f}{E} + 0.002\left(\dfrac{f}{f_y}\right)^n & \text{for } f \le f_y \\ \dfrac{f - f_y}{E_{0.2}} + \left(\varepsilon_u - \varepsilon_{0.2} - \dfrac{f_u - f_y}{E_{0.2}}\right)\left(\dfrac{f - f_y}{f_u - f_y}\right)^m + \varepsilon_{0.2} & \text{for } f_y < f \le f_u \end{cases} \tag{10}$$

$$\varepsilon = \begin{cases} \dfrac{f}{E} + 0.002\left(\dfrac{f}{f_y}\right)^n & \text{for } f \le f_y \\ \dfrac{f - f_y}{E_{0.2}} + \varepsilon_u\left(\dfrac{f - f_y}{f_u - f_y}\right)^m + \varepsilon_{0.2} & \text{for } f_y < f \le f_u \end{cases} \tag{11}$$

$$E_{0.2} = \frac{E}{1 + 0.002nE/f_y} \tag{12}$$

Based on the second stage equation, Quach and Huang [42] obtained the strain hardening exponent m by imposing the curve passing through three points: f_y, f_u, and an intermediate stress f_r (typically $f_{1.0}$ and $f_{2.0}$). This resulted in two alternative expressions for m, given by Eq. (13a) and Eq. (13b), respectively. However, the need for additional parameters reduce their practicality. When these parameters cannot be experimentally obtained, predictive expressions for them are also required.

$$m = \frac{ln\left(0.008 + \frac{f_{1.0}-f_y}{E} - \frac{f_{1.0}-f_y}{E_{0.2}}\right) - ln\left(\varepsilon_u - \varepsilon_{0.2} - \frac{f_u-f_y}{E_{0.2}}\right)}{ln\left(f_{1.0}-f_y\right) - ln\left(f_u-f_y\right)} \geq 1 \quad \text{for } f_r = f_{1.0} \tag{13a}$$

$$m = \frac{ln\left(0.018 + \frac{f_{2.0}-f_y}{E} - \frac{f_{2.0}-f_y}{E_{0.2}}\right) - ln\left(\varepsilon_u - \varepsilon_{0.2} - \frac{f_u-f_y}{E_{0.2}}\right)}{ln\left(f_{2.0}-f_y\right) - ln\left(f_u-f_y\right)} \geq 1 \quad \text{for } f_r = f_{2.0} \tag{13b}$$

Consequently, researchers have preferred to directly utilise the predictive expressions of m that have been proposed for various applicable ranges. They recognized that the strain hardening exponent m depends on the ultimate tensile strength f_u relative to the 0.2 % proof stress f_y. The following expression, Eq. (14), is obtained by employing different values of k, such as 2.8 [35], 3.3 [36], and 3.5 [32].

$$m = 1 + k\frac{f_y}{f_u} \tag{14}$$

In addressing the limitations associated with obtaining the ultimate strength f_u from experiments and improving the model's accuracy at low strains (less than approximately 10 %), Gardner and Nethercot [45] proposed adjustments to the curve in the second stage of Eq. (10), imposing the curve to pass through the 1 % proof stress $\sigma_{1.0}$ and the corresponding strain $\varepsilon_{1.0}$ in the second stage, thereby constructing Eq. (15).

$$\varepsilon = \begin{cases} \frac{f}{E} + 0.002\left(\frac{f}{f_y}\right)^n & \text{for } f \leq f_y \\ \frac{f-f_y}{E_{0.2}} + \left(\varepsilon_{1.0} - \varepsilon_{0.2} - \frac{f_{1.0}-f_y}{E_{0.2}}\right)\left(\frac{f-f_y}{f_{1.0}-f_y}\right)^{n_{0.2,1.0}} + \varepsilon_{0.2} & \text{for } f \leq f_y \end{cases} \tag{15}$$

where $n_{0.2,1.0}$ is a strain hardening coefficient representing a curve that passes through f_y and $f_{1.0}$. For similar reasons, the predictive expressions for the ultimate strength f_u and ultimate strain ε_u have also been explored. The existing expressions of the ultimate strength f_u for conventional produced steels exhibit two basic forms Eqs. (16–17), as outlined in Table 1, where e is the nondimensional proof stress (Eq. (18)). Additionally, the ultimate strain ε_u is correlated with the yield-to-ultimate stress ratio f_y/f_u, as indicated by Eq. (19) [32] and Eq. (20) [28]. Quach and Huang [42] further proposed various predictive expressions, each applicable within different ranges of n.

$$e = \frac{f_y}{E} \tag{18}$$

$$\varepsilon_u = 1 - \frac{f_y}{f_u} \tag{19}$$

Table 1
Predictive expressions of the ultimate strength σ_u following two basic forms [32,35,36,42,46].

$\frac{f_y}{f_u} = a_1 + b_1 e$	$\frac{f_u}{f_y} = a_2 + \left(\frac{b_2}{f_y}\right)^c$
$\frac{f_y}{f_u} = 0.2 + 185e$ (16a)	$\frac{f_u}{f_y} = 0.83 + \frac{203.8}{f_y}$ (17a)
$\frac{f_y}{f_u} = 0.61 + 112.94e$ (16b)	$\frac{f_u}{f_y} = 1 + \left(\frac{130}{f_y}\right)^{1.4}$ (17b)
$\frac{f_y}{f_u} = 0.46 + 145e$ (16c)	$\frac{f_u}{f_y} = 1 + \left(\frac{200}{f_y}\right)^{1.75}$ (17c)

$$\varepsilon_u = 0.6\left(1 - \frac{f_y}{f_u}\right) \tag{20}$$

In addition to the aforementioned two-stage stress-strain models, three-stage and multistage models [31–34] based on the Ramberg-Osgood model have also been proposed to achieve more accurate stress-strain response. Nevertheless, when weighing the balance between the accuracy and practicality of the stress-strain model, the two-stage model offers a broader scope of application.

2.2. Models for WAAM carbon steels

The existing tensile coupon tests and previous experiments on WAAM carbon steels conducted by the authors have shown that these steels generally exhibit stress-strain behaviour similar to conventionally produced steels (aforementioned hot-rolled and cold-formed steels). Huang et al. [39] suggested that the stress- strain curves of WAAM normal-strength steels generally aligns with the quad-linear model (Eq. (1)) or bilinear plus nonlinear hardening model (Eq. (4)), whereas the stress-strain curves of WAAM high-strength steels are more effectively described by the two-stage Ramberg-Osgood model (Eq. (10)).

However, two major differences exist. Firstly, the geometric undulations in as-built WAAM components result in reduced effective mechanical properties and introduce a certain degree of anisotropy. Therefore, prediction expressions for certain material parameters vary based on the surface conditions (machined or as-built) and the coupon extraction angles θ. Secondly, inclined yield plateaux are observed in a portion of stress-strain curves of WAAM normal-strength steels. It results in the strain hardening stress f_{sh} corresponding to the strain hardening strain ε_{sh} no longer being consistent with the yield strength f_y, as show in Fig. 7.Consequently, the second stage of Eq. (1) and (4) was modified [39] by introducing a new slope $E_p = 0.004E$.

Considering the major differences, the stress-strain curves of WAAM normal-strength steels can be classified into two categories: one with a flat yield plateau (Fig. 5), typically observed in machined coupons with various angles θ and as-built coupons with $\theta = 0^\circ$; and another with an inclined yield plateau (Fig. 7), usually seen in as-built coupons with $\theta \neq 0^\circ$. The prediction expressions for the material parameter E_{sh} and ε_u are also distinct for each case, with Eqs. (21) and (22) for the former case and Eqs. (23) and (24) for the latter case.

$$E_{sh} = \frac{f_u - f_y}{0.4(\varepsilon_u - \varepsilon_{sh})} \tag{21}$$

$$\varepsilon_u = 0.7\left(1 - \frac{f_y}{f_u}\right) \tag{22}$$

$$E_{sh} = \frac{f_u - f_y}{0.5(\varepsilon_u - \varepsilon_{sh})} \tag{23}$$

$$\varepsilon_u = \left(0.7 - \frac{0.5\theta}{\pi}\right)\left(1 - \frac{f_y}{f_u}\right) \tag{24}$$

However, other material parameters, including ε_{sh}, C_1, f_u, n, and m, were predicted using the same expression, Eqs. (25–27), regardless of the surface conditions and the coupon extraction angles.

$$\varepsilon_{sh} = 0.1\frac{f_y}{f_u} - 0.052 \quad \text{for } 0.015 \leq \varepsilon_{sh} \leq 0.03 \tag{25}$$

$$C_1 = \frac{\varepsilon_{sh} + 0.25(\varepsilon_u - \varepsilon_{sh})}{\varepsilon_u} \tag{26}$$

$$\frac{f_u}{f_y} = 1 + \left(\frac{160}{f_y}\right)^{1.4} \tag{27}$$

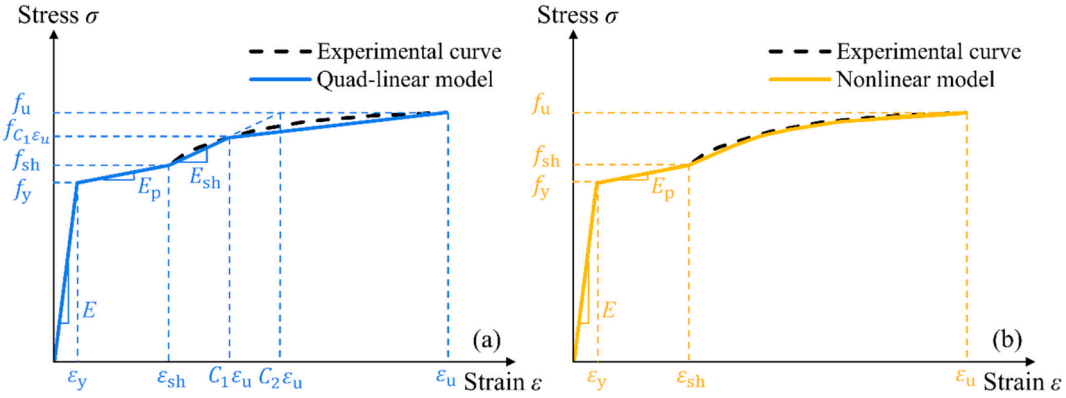

Fig. 7. Existing quad-linear and bilinear plus nonlinear hardening models for WAAM steels: (a) quad-linear model with inclined yield plateau; and (b) bilinear plus nonlinear hardening model with inclined yield plateau.

The material parameters in the model for WAAM high-strength steels, including n and m, were predicted using Eqs. (28–29).

$$n = \frac{ln(20/3)}{ln\left(\frac{f_y}{f_{0.03}}\right)} \tag{28}$$

$$m = 1 + 1.3\frac{f_y}{f_u} \tag{29}$$

3. Experimental database

Over 700 material tensile tests on WAAM steel have been collected, covering a diverse range of feedstock wires, post-treatments, surface conditions, deposition strategies, coupon extraction angles, and material thicknesses, as detailed in Table 2. The feedstock wires used include ER50–6 (specified according to GB/T 8110 [47]), ER70S-6, ER70S-G (specified according to AWS A5.18 [48]), ER90S–B3, ER90S-B91, ER100, ER100S-1, ER110S-1, ER110S-G, ER120S-G (specified according to AWS A5.28 [49]), G3Si1, G4Si1 (specified according to EN ISO 14341 [50]), XC-45 (specified according to AFNOR NF A37–502 [51]), and A-Fe-W-86 (a self-developed feedstock wire). Among these, ER70S-6 wire was the most extensively studied for WAAM applications. The deposition strategies that used to fabricate the WAAM components, including steel sheets, blocks, and sections (such as rectangular hollow sections (RHS) and circular hollow sections (CHS)) include parallel, oscillation, and dot-by-dot deposition, as depicted in Fig. 8. After fabrication, the components underwent multiple post-processes, such as heat treatment and cooling. Coupons were finally extracted from these components with various angles θ relative to the print layer direction, as shown in Fig. 9. These coupons were shaped as dog-bone sheets or round bars, with thicknesses or diameters ranging from 0.5 mm to 17 mm, and featured two surface conditions: as-built with original undulation and machined with milled surfaces, also illustrated in Fig. 10.

The quantity of material parameters and full stress-strain curves from the collected tensile coupon test data is also summarised in Table 2. Most of the material parameters were determined from the stress-strain curves digitised using software GetData [52], with a few parameters obtained directly from tables in the original manuscripts. Blank spaces in Table 2 indicate either unknown details or a zero quantity of the specified material parameter.

Among the collected stress-strain curves, 487 full stress-strain curves with discontinuous yielding were analysed to calibrate the material coefficients for the quad-linear and bilinear plus nonlinear hardening models, and 153 full stress-strain curves with continuous yielding were analysed to calibrate the strain hardening exponents n and m in the two-stage Ramberg-Osgood model. OLS regression analysis was performed to determine the model coefficients and material parameters.

It is important to note that the coupon extraction angles θ have significant influences to the material properties, particularly for WAAM as-built components. Therefore, the determination of material parameters and model coefficients was carefully adjusted to account for the effects of the angles.

4. Determination of material parameters and model coefficients

4.1. Model selection

Three typical stress-strain curves are shown in Fig. 11(a), where the curves with flat and inclined yield plateaux are the discontinuous yielding curves, and the rounded curve is the continuous yielding curve. For the discontinuous yielding curves, the updated quad-linear and bilinear plus nonlinear hardening models are proposed – see Eqs. (30) and (31), respectively.

$$f(\varepsilon) = \begin{cases} E\varepsilon & \text{for } \varepsilon \le \varepsilon_y \\ f_y + E_p\left(\varepsilon - \varepsilon_y\right) & \text{for } \varepsilon_y < \varepsilon \le \varepsilon_{sh} \\ f_{sh} + E_{sh}(\varepsilon - \varepsilon_{sh}) & \text{for } \varepsilon_{sh} < \varepsilon \le C_1\varepsilon_u \\ f_{C_1\varepsilon_u} + \dfrac{f_u - f_{C_1\varepsilon_u}}{\varepsilon_u - C_1\varepsilon_u}(\varepsilon - C_1\varepsilon_u) & \text{for } C_1\varepsilon_u < \varepsilon \le \varepsilon_u \end{cases} \tag{30}$$

$$f(\varepsilon) = \begin{cases} E\varepsilon & \text{for } \varepsilon \le \varepsilon_y \\ f_y + E_p\left(\varepsilon - \varepsilon_y\right) & \text{for } \varepsilon_y < \varepsilon \le \varepsilon_{sh} \\ f_{sh} + (f_u - f_{sh}) \times \left\{ K_1\left(\dfrac{\varepsilon - \varepsilon_{sh}}{\varepsilon_u - \varepsilon_{sh}}\right) + K_2\left(\dfrac{\varepsilon - \varepsilon_{sh}}{\varepsilon_u - \varepsilon_{sh}}\right) \Big/ \left[1 + K_3\left(\dfrac{\varepsilon - \varepsilon_{sh}}{\varepsilon_u - \varepsilon_{sh}}\right)^{K_4}\right]^{\frac{1}{K_4}} \right\} & \text{for } \varepsilon_{sh} < \varepsilon \le \varepsilon_u \end{cases} \tag{31}$$

Table 2
Summary of number and details of WAAM steel coupon test data.

Reference	Feedstock wire	Surface condition [a]	Deposition strategy [b]	Thickness/ diameter (mm)	Coupon extraction angle (°) [c]	E	f_y	f_u	ε_u	ε_{sh}	Full curves
Ahsan et al. [53]	ER70S-6 [d]	M	P	2	90°	1	4	4	1	1	1
Ahsan et al. [54]	ER70S-G [d]	M	P	1.6	0°		1	1			
Aldalur et al. [55]	ER70S-6 [d]	M	P, O	4	0°, 90°	24	24	24	24	24	24
Al-Nabulsi et al. [56]	UnionK40/ ER70S-G [d]	M	P	17	0°	3	3	3	3	3	3
Astarita et al. [57]	ER70S-6 [d]	M	P	3	0°, 90°	4	4	4	4		4
Ayana et al. [58]	ER70S-6 [d]	M	P	2	0°, 45°, 90°	6	6	6	6	6	6
Bourlet et al. [59]	ER100 [g]	M	P	4	0°		24	24			
Chen et al. [14]	ER100S-G [g], ER110S-G [g], ER120S-G [g]	M, AB	P	6.5	0°, 30°, 45°, 60°, 90°	60	60	60	60	16	60
Dirisu et al. [15]	ER70S-6 [d], ER90S–B3 [g], ER120S-G [g]	M	P	3	0°, 90°	6	6	6	6	2	6
Ermakova et al. [60]	ER100S-1 [g], ER70S-6 [d]	M	O	8	0°, 90°	4	4	4	4	2	4
Fang et al. [61]	800 MPa class [i]	M	P	5	0°, 90°	6	6	6	6	1	6
Ghaffari et al. [62]	ER70S-6 [d]	M	P	5	0°, 90°	2	2	2	2	2	2
Guo et al. [63]	ER70S-6 [d]	M, AB	P	3, 8	0°, 45°, 90°	27	27	27	27	27	27
Guo et al. [64]	SRSF690M [i]	M	P		0°, 90°		2	2			
Huang et al. [12]	ER70S-6 [d], ER110S-G [g]	M, AB	P	3, 8	0°, 30°, 45°, 60°, 90°	137	137	137	137	116	137
Huang et al. [65]	ER70S-6 [d]	M, AB	P	3	90°	4	4	4	4	3	4
Karabulut et al. [66]	3Dprint AM35/ ER70S-G [d]	M	O	12	0°, 90°	6	6	6	6	2	6
Khandelwal et al. [67]	ER70S-6 [d]	M	P	10	0°, 90°	4	4	4	4	4	4
Kotteman et al. [68]	ER70S-6 [d]	M, AB	P	1.5–6	0°, 45°, 90°	60	60	58	58	58	60
Kühne et al. [69]	G3Si1 [e]	AB	P	8	0°, 90°	2	2	2	2	2	2
Kumar et al. [70]	ER70S-6 [d]	M	P		90°	9	9	9	9		9
Kyvelou et al. [71]	ER70S-6 [d]	AB	P	6.5	0°	4	4	4	4	4	4
Laghi et al. [13]	ER70S-6 [d]	M	O	4	0°, 45°, 90°	24	24	24	24	24	24
Lange et al. [72]		M	P		90°	7	7	7	7	7	7
Le et al. [73]	ER70S-6 [d]	M	P	2	0°, 90°	6	6	6	6	6	6
Li et al. [16]	ER90S-B91 [g]	M	P		90°	2	2	2	2		2
Lin et al. [74]	XC-45 [h]	M	P		0°, 90°		4	4			
Liu et al. [22]	ER50–6 [f]	M, AB	P	3, 5, 8	0°, 45°, 90°	52	52	52	52	52	52
Lu et al. [75]	ER70S-6 [d]	M	P	0.5	0°, 90°	6	6	6	6	6	6
Ma et al. [76]	ER50–6 [f]	M	P	1.2	0°	4	4	4	4	4	4
Michl et al. [77]	ER70S-6 [d]	M	P	4	0°, 45°, 90°	11	11	11	11	10	11
Müller et al. [17]	G4Si1 [e]	AB	D	8.2, 9.16, 10	90°	3	3	3	3	2	3
Müller et al. [78]	3Dprint AM80/ ER110S-1 [g]	M	P	3	0°		46	46			
Nagasai et al. [79]	ER70S-6 [d]	M	P	4	90°	2	2	2	2	2	2
Nemani et al. [18]	ER70S-6 [d]	M	P	5	0°, 90°	6	6	6	6	4	6
Rafieazad et al. [80]	ER70S-6 [d]	M	P		0°, 45°, 90°	3	3	3	3	2	3
Raut et al. [81]	ER70S-G [d]	M	P	4	0°	1	2	2	1	1	1
Rodrigues et al. [82]	ER110S-G [g]	M	P	4	0°, 90°	4	4	4	4		4
Ron et al. [83]	ER70S-6 [d]	M	P	3.81	90°	1	1	1	1	1	1
Silvestru et al. [84]	Union SG 2-H/ ER70S-6 [d]	M	D	5.5	45°, 90°	15	15	15	15	15	15
Song et al. [85]	ER70S-6 [d]	M, AB	P	4, 8	0°, 45°, 90°	24	24	24	24	24	24
Song et al. [86]	ER70S-6 [d]	M, AB	P	6	0°, 90°	10	10	10	10	10	10
Sun et al. [87]	A-Fe-W-86 [i]	M	P	2	0°, 90°	2	6	6	2		2
Tankova et al. [88]	ER70S-6 [d]	M, AB	P	8	0°, 45°, 90°	18	18	18	18	18	18
Tripathi et al. [89]	ER70S-6 [d]	M	P	4	0°, 90°	2	2	2	2		2
Weber et al. [90]	ER110S-G [g]	M, AB	P	8	0°, 22.5°, 45°, 67.5°, 90°	60	60	60	60	18	60
Webster et al. [91]	ER100S-G [g]	M	P	6.1	90°	3	3	3	3		3
Xin et al. [92]	ER70S-6 [d]	M	P	2.8	0°, 45°, 90°	8	8	8	8	8	8
Yildiz et al. [93]	ER120S-G [g]	M	P, O	3.3	0°, 90°	5	5	5	5		5
Total						648	733	731	646	487	640

[a] M = Machined, AS = as-built.

[b] P = Parallel deposition strategy; O = Oscillation deposition strategy; D = Dot by dot deposition strategy.
[c] Coupon extraction angles = Angles between the specimen axis and the print layer orientations during manufacturing.
[d] Specified according to AWS A5.18 [48].
[e] Specified according to EN ISO 14341 [50].
[f] Specified according to GB/T 8110 [47].
[g] Specified according to AWS A5.28 [49].
[h] Specified according to AFNOR NF A37–502 [51].
[i] Self-developed feedstock wires.

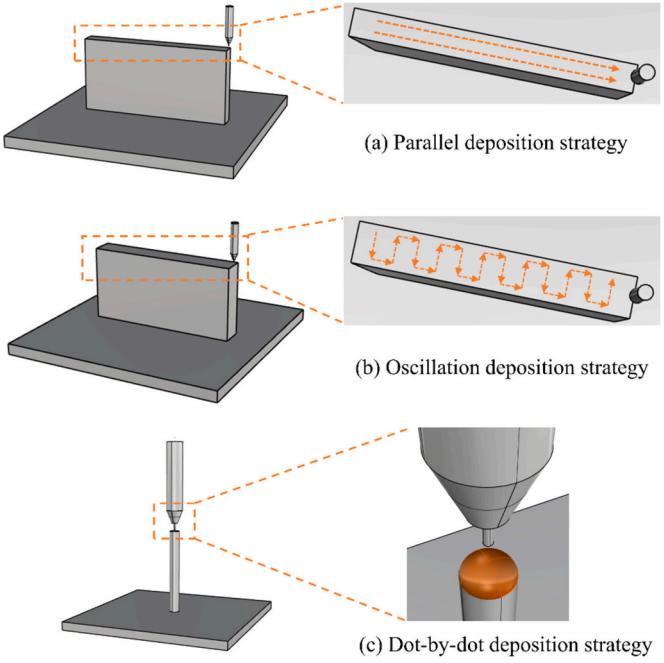

Fig. 8. Illustration of deposition strategy.

where $E_p = 0$ with flat yield plateau, and $E_p = 0.007E$ with inclined yield plateau (see Section 4.5.2 for detailed discussion). Meanwhile, for the continuous yielding curves Ramberg-Osgood model (i.e. Eq. (10)) is adopted for calibration. The proposed stress-strain models incorporate three fundamental material parameters: the Young's modulus E, yield strength f_y, and ultimate strength f_u, which are assumed to be known in most cases. The remaining material parameters were derived using predictive expressions fitted to the collected database, resulting in models suitable for WAAM steels, which will be discussed in the following sections.

The occurrence of different yield plateau and corresponding model selection is a very worthwhile topic for discussion. As shown in Fig. 11 (b), in the overall database, the three types of yielding response, including flat, inclined, and rounded yield plateaux, account for 59 %, 15 %, and 26 %, respectively. The WAAM steels with f_y smaller than 500 MPa tend to exhibit discontinuous yielding with 93 % of them have flat

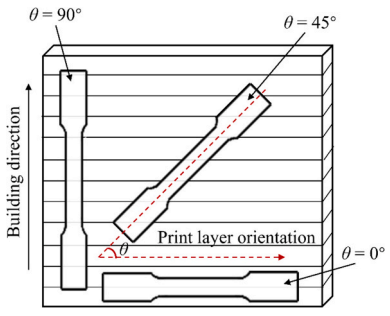

Fig. 9. Illustration of coupon extraction angle θ.

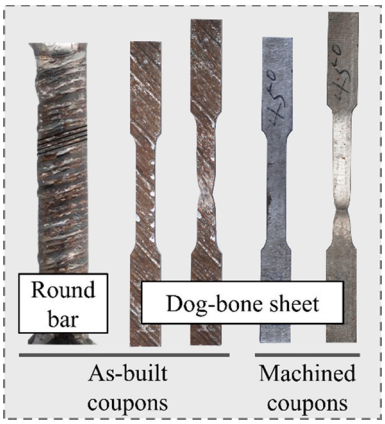

Fig. 10. Illustration of coupon surface condition.

or inclined yield plateaux, while the ones with f_y larger than 500 MPa tends to exhibit continuous yielding, with 74 % of them have rounded non-plateau. If only the yield strength is used as a criterion for determining the occurrence of a yield plateau, it seems impossible to cover all cases.

Wang et al. [38] believed that the yield strength of the high strength steel and its carbon content determined the occurrence of the yield plateau. Accordingly, Fig. 12(a) illustrates the effects of yield strength and carbon content on the occurrence of yield plateau for different yielding responses of WAAM steel. Two criteria, listed in Table 3, are drawn in green dash lines as the boundary for curves with yield plateau and without yield plateau.

To evaluate the accuracy of the two criteria, the ratio of the number of data with yield plateau located below the boundary line to the total number of data with yield plateau $\frac{n_{\text{plateau\_below}}}{n_{\text{plateau\_all}}}$, as well as the ratio of the number of data without yield plateau located above the boundary line to the total number of data without yield plateau $\frac{n_{\text{non-plateau\_above}}}{n_{\text{non-plateau\_all}}}$, were calculated. The slightly difference of average accuracy shows that the criterion No.1 which considers the effect of an extra factor of carbon content is almost consistent with the criterion No.2 which only considers yield strength.

Further considering the characteristics of WAAM steels compared with conventional produced steels, the coupon extraction angle, surface condition, and deposition strategy of WAAM steels may have potential effects on the yielding response, as shown in Fig. 12 and Table 3. A similar conclusion can be drawn that there is not much difference between the two criteria. Therefore, considering the balance between accuracy and convenience, yield strength can be utilised to distinguish yielding responses. Note that the average accuracy of this criterion is 84.1 %, and further research could be conducted to optimise it.

Note that the criterion for distinguishing the flat or inclined yield plateau is also worthy discovering. Considering different factors, including coupon extraction angle, surface condition, and deposition strategy, the distributions of each yielding response are shown in Fig. 13. The proportion in each ring is marked only if it is not less than 5 %. For the collected database of WAAM steels with yield strength f_y below 500 MPa, the specimens with angle of 90°account for 62 %, the as-built specimens account for 91 %, and the specimens manufacturing by

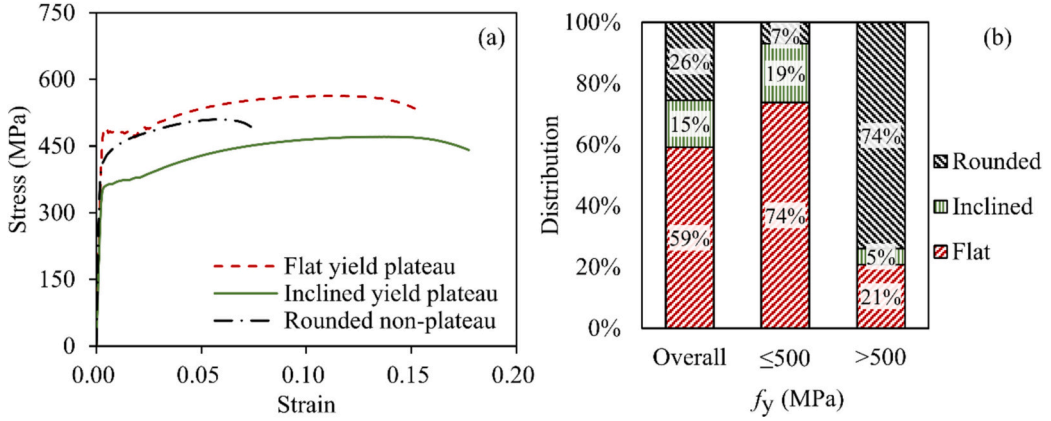

Fig. 11. The stress-strain curves and distribution of yield responses in the WAAM steel database.

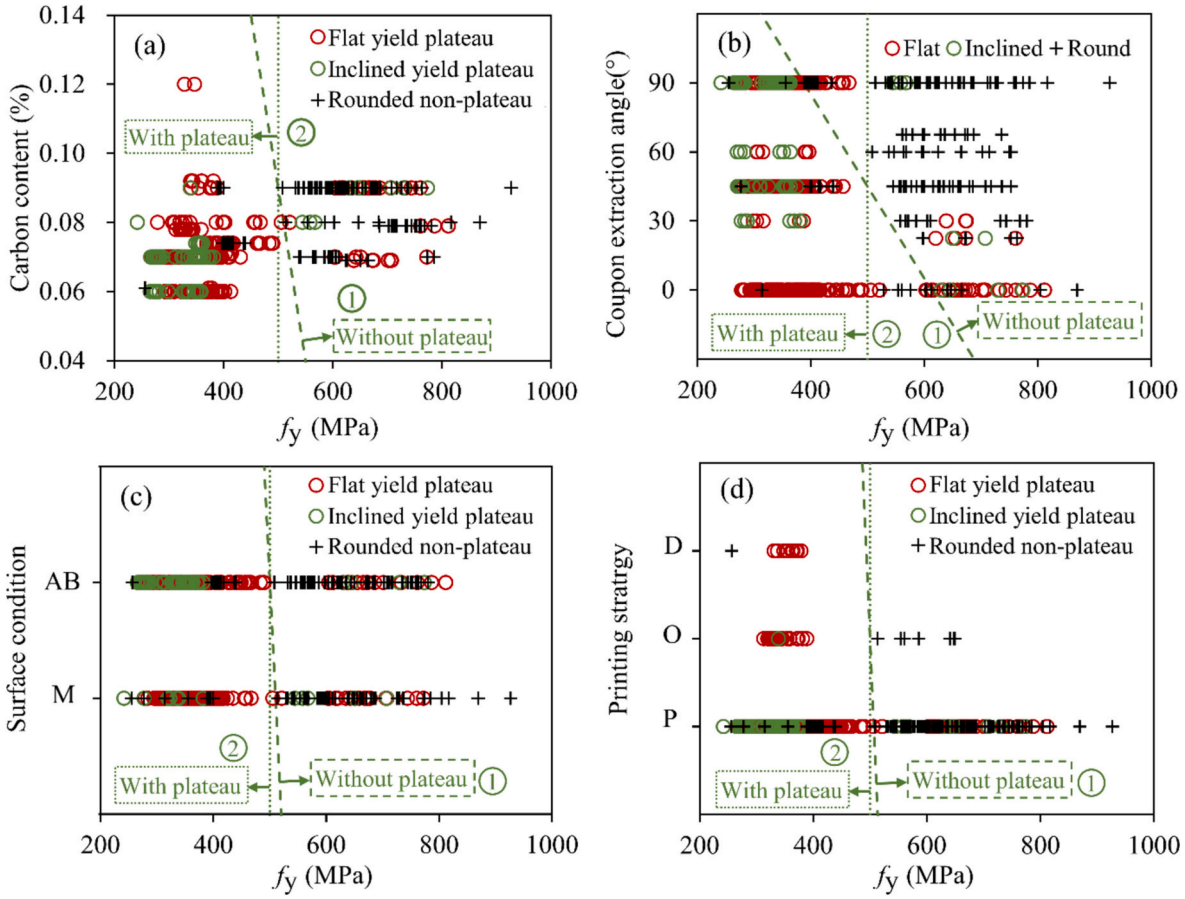

Fig. 12. Effects of yield stress f_y and (a) carbon content, (b) coupon extraction angle, (c)surface condition, and (d) deposition strategy on the yielding response of WAAM steels.

parallel deposition strategy account for 99 % the inclined yield plateau data.

As shown in Fig. 13(a), the specimens with inclined yield plateau have angles of not less than 30°, accounting for 8 %, 23 %, 7 % and 62 % respectively, and the majority of the surface conditions of these specimens are in as-built. Considering that the material properties of as-built specimens with an angle of 0° are similar to those of machined specimen [12,39], it seems that it can be concluded that as-built specimens with an angle other than 0° usually show inclined yield plateau. However, in the specimens with flat yield plateau, as-built specimens with an angle greater than 0° also account for a proportion that cannot be ignored, so the above conclusion is only a necessary and insufficient condition. A similar conclusion can also be obtained from Fig. 13(b). As for the influence of deposition strategy, due to the small amount of data except for parallel deposition strategy, and the majority of the specimens are flat yield plateau, it is considered that it has little impact on the yield plateau as shown in Fig. 13(c).

Summarily, for WAAM specimens with yield strength greater than 500 MPa, the continuous stress-strain model with rounded yield plateau (two-stage Ramberg-Osgood model) is preferred; for WAAM specimens with yield strength less than 500 MPa, the discontinuous stress-strain model with inclined yield plateau (quad-linear model/ bilinear plus

Table 3
Criteria for determining the occurrence of a yield plateau according to different factors.

Boundary	Factors	Criteria	$\frac{n_{\text{plateau\_below}}}{n_{\text{plateau\_all}}}$	$\frac{n_{\text{non-plateau\_above}}}{n_{\text{non-plateau\_all}}}$	Average accuracy
1	Carbon content	$\text{C\%} = 0.09 - 0.001 \times (f_y - 500)$	80.4 %	81.0 %	80.7 %
	Coupon extraction angle	$\theta = 45 - 0.4 \times (f_y - 500)$	85.2 %	89.4 %	87.3 %
	Surface condition	$\text{SC}(1,2) = 2 - 0.1 \times (f_y - 500)$	90.6 %	80.0 %	85.3 %
	Deposition strategy	$\text{DS}(1,2,3) = 2 - 0.15 \times (f_y - 500)$	90.6 %	80.0 %	85.3 %
				Total average accuracy	84.7 %
2	Carbon content	$f_y = 500$	80.2 %	81.0 %	80.6 %
	Coupon extraction angle		90.4 %	80.0 %	85.2 %
	Surface condition		90.4 %	80.0 %	85.2 %
	Deposition strategy		90.4 %	80.0 %	85.2 %
				Total average accuracy	84.1 %

nonlinear hardening model) is suitable for specimens with $\theta \neq 0^{\circ}$ in as-built specimens, and the discontinuous stress-strain model proposed with flat yield plateau (quad-linear model/bilinear plus nonlinear hardening model) can be used in other cases. However, it is worth noting that a large number of as-built specimens with $\theta \neq 0^{\circ}$ may be more fitted to the discontinuous stress-strain model with flat yield plateau, which requires subsequent simulation for error analysis.

4.2. Young's modulus E

The Young's modulus E extracted from literatures varies from 2 to 1600 GPa – see Fig. 14(a). The Young's modulus is determined by regression analysis, as described in [9]. A typical example of the adopted method is shown in Fig. 15. Since experimental noise is often present in stress-strain curves, the numerical derivative cannot be computed directly. To address this, a moving regression filter is applied to smooth the curve, and the Young's modulus E is calculated at each point, as illustrated in Fig. 15(a). The computed values of E are then plotted against the corresponding strain values (averaged across the regression window), as shown in Fig. 15(b). The Haar wavelet transform [94] is employed to identify the positions of the ramp-up and ramp-down regions in E, which define the bounds of a window (bands A and B in Fig. 15(b)) containing a plateau region of constant E. Within this plateau region, an S-shaped logistic curve is fitted to the data using the Levenberg-Marquardt nonlinear least squares regression algorithm [95,96]. Finally, the Young's modulus E is determined as the value of the fitted logistic curve at the strain corresponding to band A, which is denoted by the red point in Fig. 15(b).

In order to eliminate the errors raised from the extraction process or other potential reasons, only the values between 100 and 300 GPa were considered, as the data point between the grey dash lines. As depicted in Fig. 14(b), the Young's modulus values of WAAM steels were slightly sensitive to the surface conditions and coupon extraction angles. The average Young's modulus values for WAAM as-built and machined carbon steel coupons were 202 GPa and 192 GPa respectively, with both of them lower than the value 210 GPa given in EN1993-1-1 [97] and 203 GPa recommended in AISI [98].

4.3. Ultimate strength f_u

As discussed in Section 2.1.1, the ultimate strength f_u is generally estimated using two types of predictive expressions: Eqs. (16a-c) and (17a-c), derived from regression analyses in previous studies. Focused on the latter type of expression and conducted preliminary analysis using the collected test data (summarised in Table 2), the ratios of f_u/f_y are plotted against the yield strength f_y in Fig. 16(a).

The variations in f_u/f_y with f_y for WAAM steels can be classified into three categories, influenced by the type of feedstock wires (primarily corresponding to yield strength f_y), heat treatments, and interpass temperatures during manufacturing process. The majority of coupons, manufactured using either low- or high-strength feedstock wires, follow a consistent trend and are classified into Category 1. Notably, in a specific experiment within Category 1, the interpass temperature was abnormally high, exceeding the maximum allowable limit of 350 °C specified in EN 1011–2 [99]. This anomaly resulted in reduced yield strengths, causing these samples to deviate from their original group and form a new subset within Category 2. Category 2 consists of a part of coupons with yield strengths exceeding 500 MPa, which exhibit a distinct trend compared to Category 1. However, the reasons for the occurrence of two branches in coupons made of high-grade strength feedstock wires, excluding the influence of interpass temperature, remain unclear and require further investigation with additional data. Category 3 is unique, as the data in this group is derived from experiments in Category 2. However, additional heat treatment during manufacturing led to a decrease in f_u/f_y, in line with the trend observed in Category 1. In summary, these three categories can be reclassified into two major categories that reflect two distinct trends, which can be predicted using two different design expressions given by Eqs. (32a) and (32b), as shown in Fig. 16(b).

$$\frac{f_u}{f_y} = 1 + \left(\frac{150}{f_y}\right)^{1.3} \quad \text{for Category 1} \tag{32a}$$

$$\frac{f_u}{f_y} = 1 + \left(\frac{360}{f_y}\right)^{1.5} \quad \text{for Category 2} \tag{32b}$$

In addition, the variations in f_u with f_y for WAAM steels are illustrated in Fig. 17(a), following the same distribution pattern as shown in Fig. 16(a). A new predictive expression for the ultimate tensile strength f_u is also proposed as Eqs. (33a) and (33b) in Fig. 17(b).

$$f_u = f_y + 115 \quad \text{for Category 1} \tag{33a}$$

$$f_u = f_y + 285 \quad \text{for Category 2} \tag{33b}$$

The key statistical values, including the mean and COV of the predicted-to-test results $f_{u,\text{pred}}/f_{u,\text{test}}$, determined from the existing Eq. (27) for WAAM steels and the proposed Eqs. (32) and (33), are summarised in Table 4. The predictive expressions Eqs. (32) and (33) both provide strong average predictions of the test data, with the mean ratios of the predicted-to-test values close to 1.0. Eq. (27) [39] also demonstrates high prediction accuracy, yielding the predicted-to-test values of 0.960 for data in Category 1, but performs significantly worse for data in Category 2. This proves the superiority of the proposed expressions.

Overall, Eqs. (32) and (33) accurately predict the ultimate tensile strength f_u of WAAM carbon steels, with Eq. (32) being the preferred choice due to its conservatism. Additionally, when it is uncertain which categories the coupons belong to, the newly proposed Eq. (34), derived from the complete experimental dataset, provides a reliable predictive

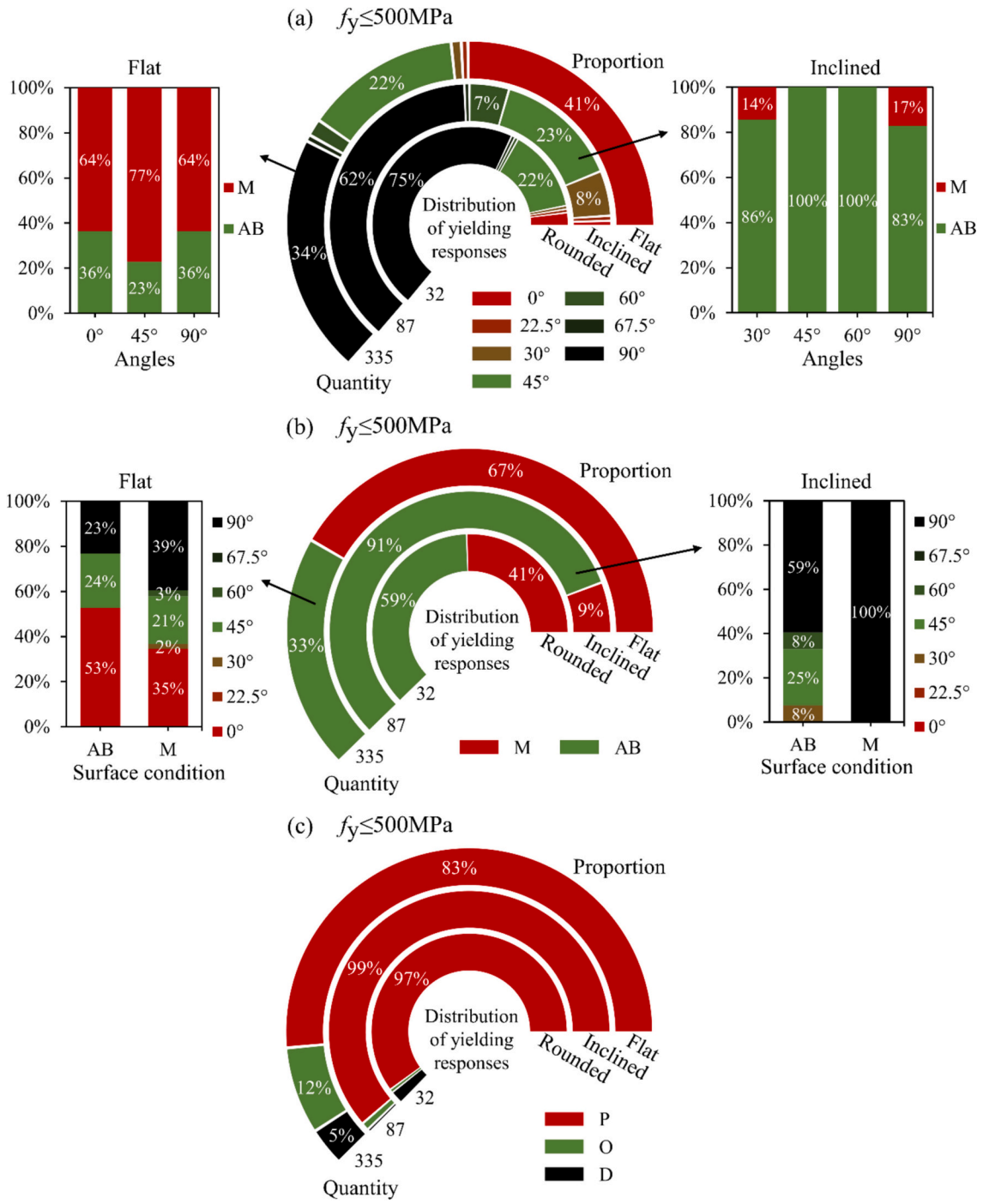

Fig. 13. The distribution (proportion and quantity) of yielding responses: (a) coupon extraction angle, (b)surface condition, and (c) deposition strategy.

expression. It achieves a mean predicted-to-test ratio of 0.995 with a COV of 0.073, ensuring trustworthy and consistent predictions. The observed presence of two distinct branches within the coupons exhibiting yield strengths f_y exceeding 500 MPa remains inadequately understood currently. Consequently, further research is needed based on more WAAM stress-strain data.

$$\frac{f_u}{f_y} = 1 + \left(\frac{90}{f_y}\right)^{0.8} \tag{34}$$

4.4. Ultimate strain ε_u

The ultimate strain ε_u collected from the literatures are plotted against the corresponding f_y/f_u ratios for as-built and machined coupons in Figs. 18(a) and 18(b) respectively, where the proposed respective equations Eqs. (35a) and (35b) are also illustrated. Meanwhile, for both proposed equations, the extraction angles are considered.

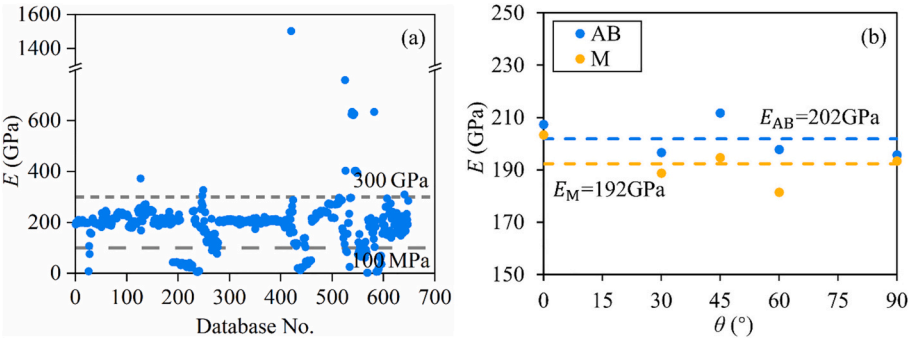

Fig. 14. The obtained Young's modulus E database: (a) values, and (b) averages according to angles and surface conditions.

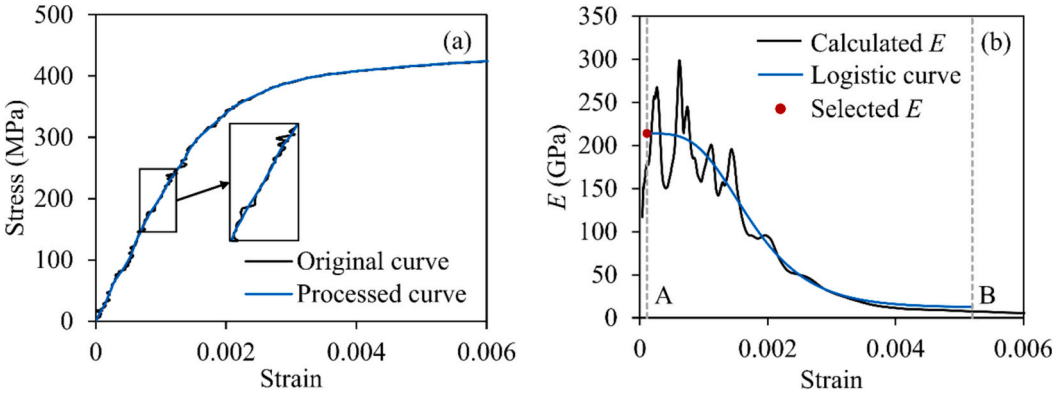

Fig. 15. Process for the determination of the Young's modulus E.

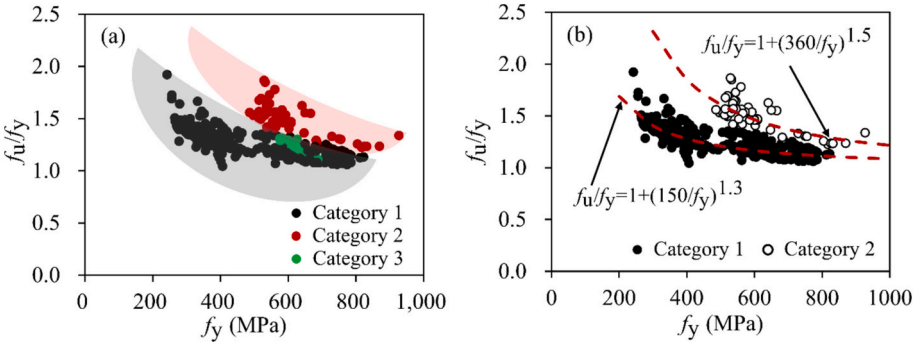

Fig. 16. (a) The variations of f_u/f_y with f_y and (b) predictions of the yield strength f_y using Eq. (32).

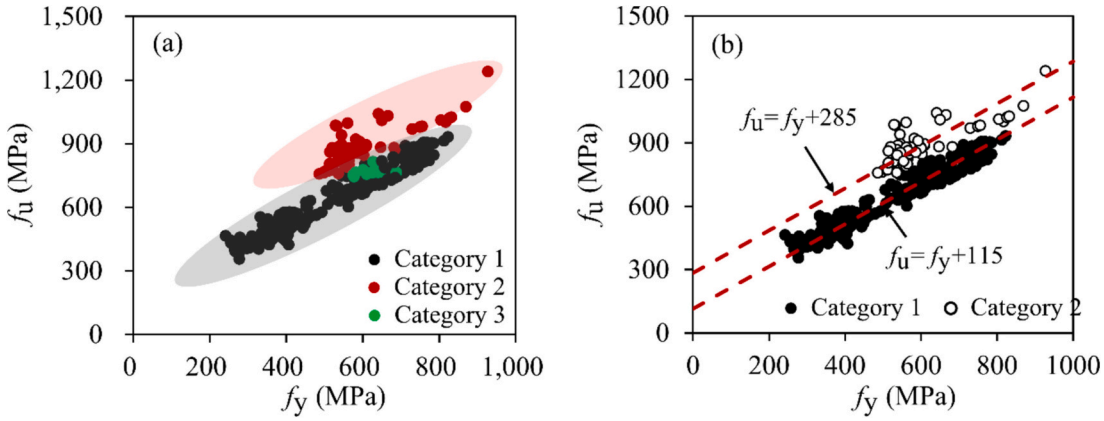

Fig. 17. (a) The variations of f_u with f_y and (b) predictions of the yield strength f_y using Eq. (33).

Table 4
Statistical results of $f_{u,pred}/f_{u,test}$ using different predictive expressions.

	$f_{u,pred}/f_{u,test}$					
Scope	Category 1			Category 2		
Equation	Eq. (27)	Eq. (32a)	Eq. (33a)	Eq. (27)	Eq. (32b)	Eq. (33b)
Mean	0.960	0.995	0.999	0.784	0.996	0.999
COV	0.043	0.043	0.045	0.077	0.061	0.066

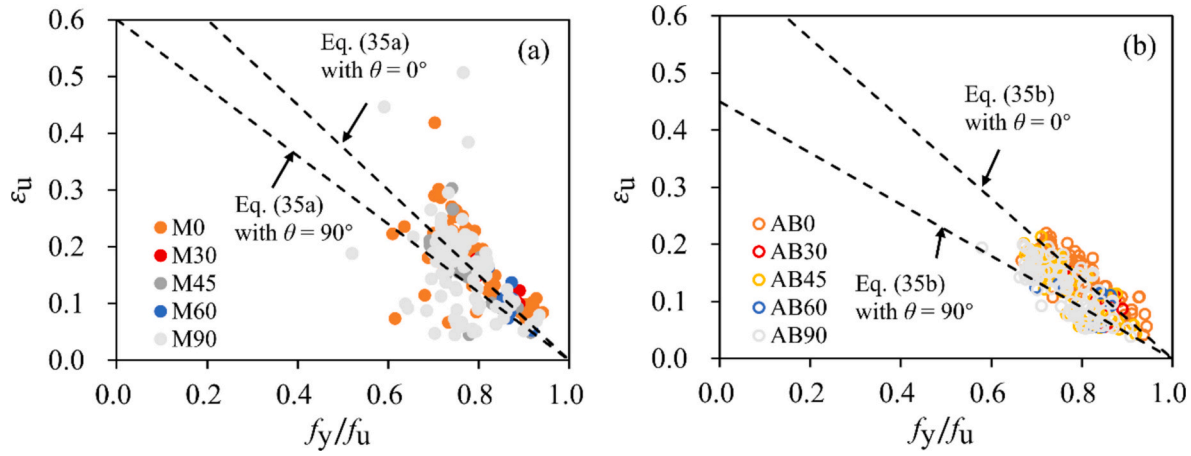

Fig. 18. Assessment of predictive expressions for ultimate strain ε_u for (a) as-built and (b) machined WAAM steels.

Table 5
Statistical results of $\varepsilon_{u,pred}/\varepsilon_{u,test}$ using different predictive expressions.

	$\varepsilon_{u,pred}/\varepsilon_{u,test}$				
	Machined	As-built		Overall	
Equation	Eq. (22) / Eq. (35a)	Eq. (24)	Eq. (35b)	Eq. (22) / Eq. (24)	Eq. (35)
Mean	0.997	1.056	0.998	1.028	0.997
COV	0.262	0.483	0.455	0.401	0.376

$$\varepsilon_u = \left(0.75 - \frac{0.3\theta}{\pi}\right)\left(1 - \frac{f_y}{f_u}\right) \quad \text{for machined WAAM steels } (\theta \text{ in rad}) \tag{35a}$$

$$\varepsilon_u = \left(0.7 - \frac{0.5\theta}{\pi}\right)\left(1 - \frac{f_y}{f_u}\right) \quad \text{for as-built WAAM steels } (\theta \text{ in rad}) \tag{35b}$$

The predictive expression Eq. (35a) yields reliable predictions for the test data, exhibiting a conservative bias with a mean ratio of the overall tested-to-predicted values of 0.997 and a moderate COV of 0.376, as detailed in Table 5. For as-built coupons, the proposed Eq. (35b) predicts the ultimate strain ε_u more accurately and conservatively than Eq. (24), with predicted-to-test ratios of 0.998 versus 1.056, making it more suitable for application requirements.

4.5. Material parameters of a model with discontinuous yielding

4.5.1. Strain hardening strain ε_{sh}

The measured strain hardening strains ε_{sh} for both machined and as-built WAAM steel coupons are plotted against the ratio of f_y/f_u in Fig. 19. Based on regression analysis and using an expression similar in format to Eq. (3), the unified equation Eq. (36) was proposed to predict ε_{sh} for

Table 6
Statistical results of $\varepsilon_{sh,pred}/\varepsilon_{sh,test}$ using different predictive expressions.

	$\varepsilon_{sh,pred}/\varepsilon_{sh,test}$				
	Overall			Machined	As-built
Equation	Eq. (25)	Eq. (36)	Eq. (37)	Eq. (37a)	Eq. (37b)
Mean	0.905	1.021	1.014	1.009	1.019
COV	0.408	0.369	0.364	0.348	0.381

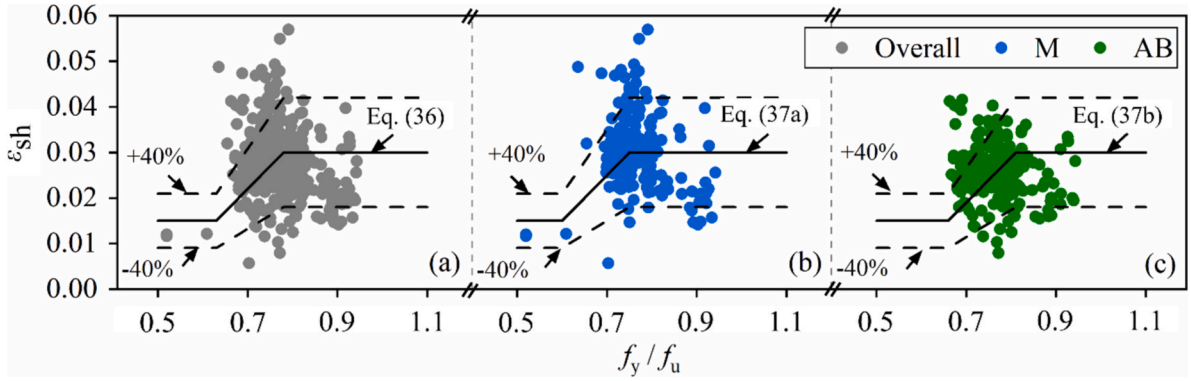

Fig. 19. Evaluation of predictive expressions for ε_{sh} for (a) overall, (b) machined, and (c) as-built WAAM steels.

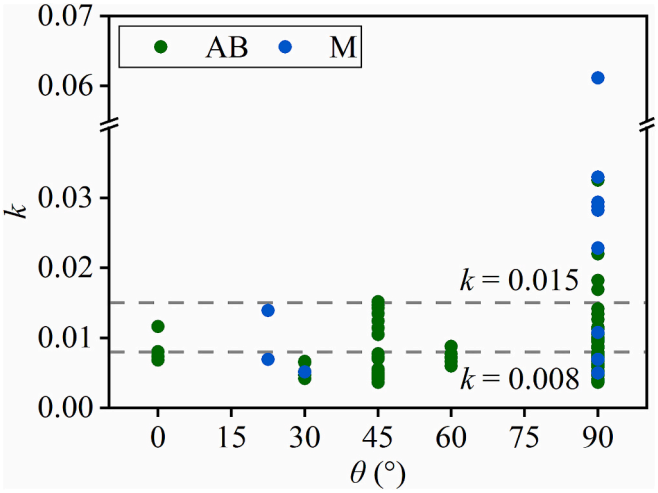

Fig. 20. The coefficient k in inclined yield plateau slope E_p of database.

WAAM carbon steels. As shown in Fig. 19(a), although the coupon test results for ε_{sh} are relatively scattered, the proposed unified expression Eq. (36) provides accurate predictions for all WAAM steel coupons, capturing over 80 % of the test data within ±40 %.

$$\varepsilon_{sh} = 0.1\frac{f_y}{f_u} - 0.048 \quad \text{for } 0.015 \le \varepsilon_{sh} \le 0.03 \tag{36}$$

Figs. 19(b) and 19(c) reveal that machined WAAM steel coupons generally have larger strain hardening strains ε_{sh} compared to as-built WAAM steel coupons. To account for the effect of surface conditions, Eq. (37) were proposed.

$$\varepsilon_{sh} = 0.1\frac{f_y}{f_u} - 0.045 \text{ for } 0.015 \le \varepsilon_{sh} \le 0.03 \text{ for machined WAAM steels} \tag{37a}$$

$$\varepsilon_{sh} = 0.1\frac{f_y}{f_u} - 0.051 \text{ for } 0.015 \le \varepsilon_{sh} \le 0.03 \text{ for as}-\text{built WAAM steels} \tag{37b}$$

The key statistical values for ε_{sh}, determined from the existing Eq. (24) for WAAM steels and the proposed Eq. (36) and (37), are summarised in Table 6. The comparison results demonstrate that, despite a minor modification to one of the model coefficients, the proposed Eq. (36) enhances the prediction accuracy for ε_{sh} compared to Eq. (25), achieving a mean predicted-to-test ratio value of ε_{sh} equal to 1.021 and a reduced COV of 0.369. Additionally, considering the effect of surface conditions, Eq. (37) provides more precise predictions, with a mean predicted-to-test ratio value of 1.014 and a further reduced COV of 0.364.

4.5.2. *Inclined yield plateau slope E_p of a linear model*

A total of 96 experimental stress-strain curves with inclined yield have been analysed to obtain the slope E_p which is defined as Eq. (38).

$$E_p = kE \tag{38}$$

The coefficient k was determined by fitting data from yield stress f_y to strain hardening stress f_{sh} for each stress-strain curve. The fitted results are depicted in Fig. 20 against the coupon extraction angle θ.

Fig. 20 shows the coefficient k values collected from literatures regarding to the different extraction angles. Although only limit data were collected from machined coupons which are somewhat scattered with a mean value of 0.015, the data collected as-built coupons have a more stable trend regardless the extraction with an average value of 0.008.

Noting that the stress-strain model with inclined yield plateau is utilised for WAAM as-built coupon with coupon extraction angle $\theta \neq 0^\circ$ discussed in model selection. The average k value of as -built coupons with $\theta \neq 0^\circ$ is 0.007. Therefore, considering conservatism and applicability, $k = 0.007$ is utilised as the final predictive expression. The k value is larger than the 0.004 proposed by Huang et al. [28] due to the utilisation of an expanded database. In summary, the following equation is obtained as Eq. (39a) and (39b).

$$E_p = 0 \text{ for flat yield plateau} \tag{39a}$$

$$E_p = 0.007E \text{ for inclined yield plateau} \tag{39b}$$

4.5.3. *Material coefficients*

A total of 414 experimental stress-strain curves exhibiting discontinuous yielding, covering 257 machined and 210 as-built WAAM steel coupons, have been collected and analysed to establish predictive expressions for the material coefficients (C_1 and E_{sh}) employed in the quad-linear model (Eq. (30)) and to calibrate the material coefficients (K_1, K_2, K_3 and K_4) used in the bilinear plus nonlinear hardening model (Eq. (31)).

Since the purpose of the curve fitting was to achieve an accurate description of the strain hardening properties, the data from the elastic and yield plateau regions of the curves (i.e. below ε_{sh}) were discarded. After applying the curve fitting approach described in Section 2.1.1, the strain hardening regions of the test stress-strain curves were represented with an evenly distributed set of data points, which were utilised for the following fitting process. The strain hardening region of the fitted data points of both the machined and as-built coupons with different coupon extraction angles are plotted in a normalised form in Fig. 21(a) and Fig. 22(a).

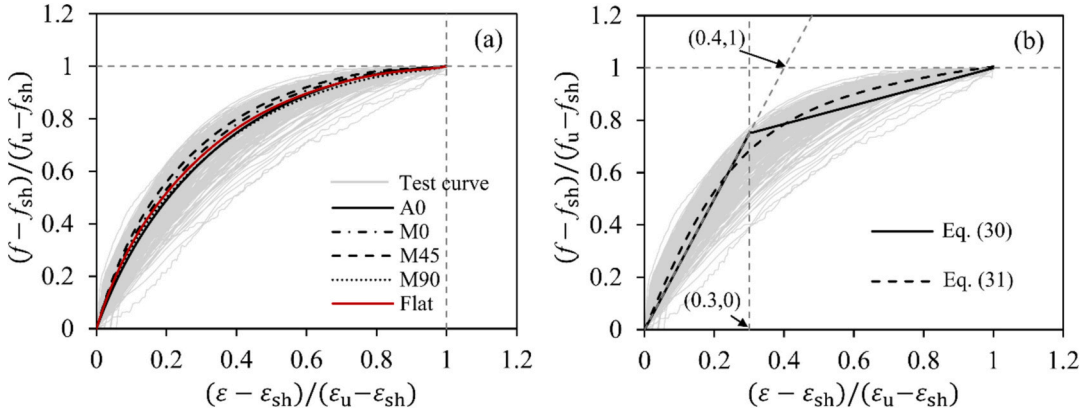

Fig. 21. The strain hardening region of (a) the fitted curves and (b) the proposed nonlinear and quad-linear models with flat yield plateau.

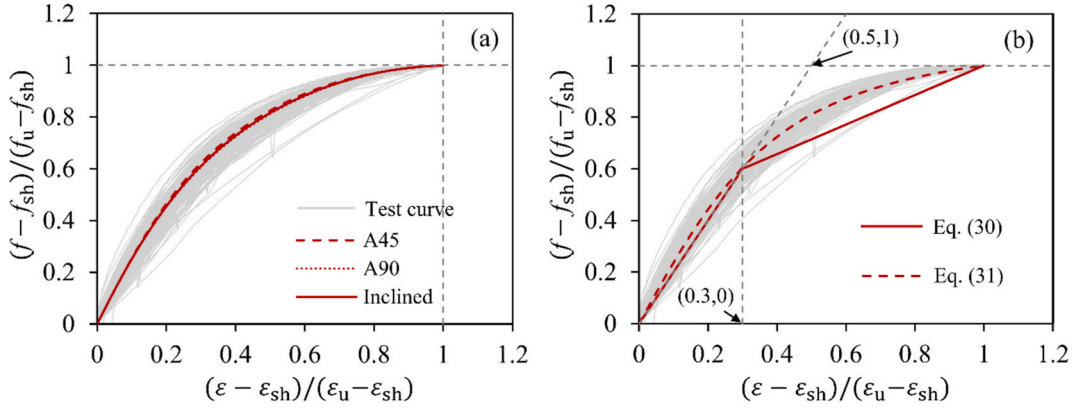

Fig. 22. The strain hardening region of (a) the fitted curves and (b) the proposed nonlinear and quad-linear models with inclined yield plateau.

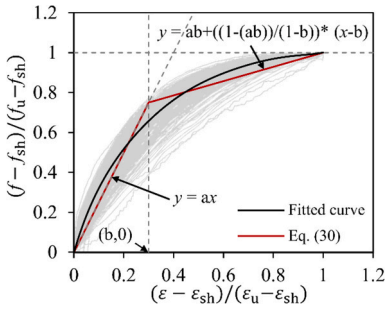

Fig. 23. The fitting process of the quad-linear model.

The material coefficients (C_1 and E_{sh}) in the quad-linear model and the material coefficients (K_1, K_2, K_3 and K_4) in the bilinear plus nonlinear hardening model for different yielding responses were determined by means of OLS regression analysis. The following predictive expressions for the material coefficients C_1 and E_{sh} were obtained through the fitting process illustrated in Fig. 23:

$$C_1 = \frac{\varepsilon_{sh} + 0.3(\varepsilon_u - \varepsilon_{sh})}{\varepsilon_u} \tag{40}$$

$$E_{sh} = \frac{f_u - f_y}{0.4(\varepsilon_u - \varepsilon_{sh})} \text{ for flat yield plateau} \tag{41a}$$

$$E_{sh} = \frac{f_u - f_y}{0.5(\varepsilon_u - \varepsilon_{sh})} \text{ for inclined yield plateau} \tag{41b}$$

Different sets of material coefficients are proposed for the stress-strain model with flat yield plateau (K1 = 0.1, K2 = 3, K3 = 10 and K4 = 2) and the stress-strain model with inclined yield plateau (K1 = 0.02, K2 = 2.4, K3 = 5 and K4 = 2), in accordance with their different strain hardening behaviour, as indicated in Fig. 21(b) and Fig. 22(b), respectively. It can be observed from Fig. 21(b) and Fig. 22(b) that the proposed predictive expressions can accurately capture the strain hardening behaviour of WAAM steels.

4.6. Material parameters of a model with continuous yielding

4.6.1. Strain hardening exponent n

The test values of the first strain hardening exponent n, as shown in Fig. 24(a), can be obtained by fitting on the experimental stress-strain

Table 7
Statistical results of n_{pred}/n_{test} using different predictive expressions.

n_{pred}/n_{test}	Eq. (9)	Eq. (28)	Eq. (42)
Mean	1.103	0.901	0.991
COV	0.128	0.141	0.107

Table 8
Recommended representative values for strain hardening exponents n and m.

	n	m
Machined coupons	14.9	2.3
As-built coupons	15.2	2.7
Overall	15.0	2.5

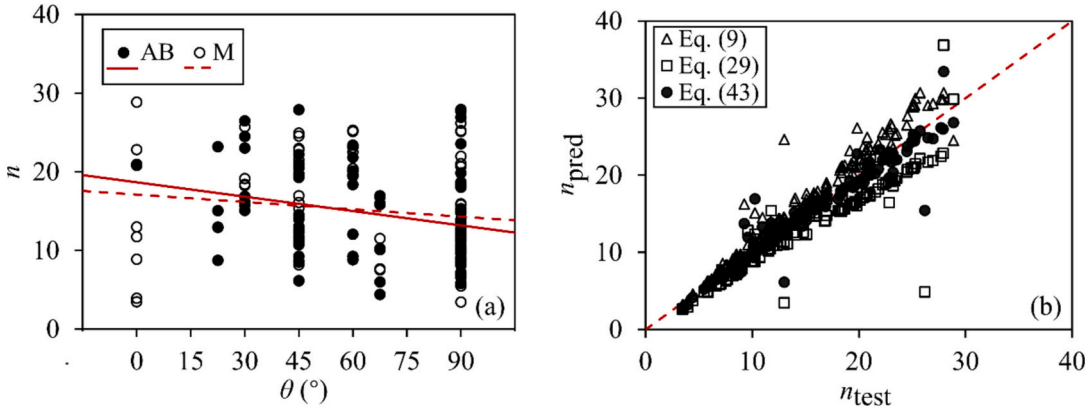

Fig. 24. (a) Distribution of the first strain hardening exponent n at different angles, and (b) evaluation of predictive expressions for n for WAAM steels when measured $\sigma_{0.03}$, $\sigma_{0.04}$ and $\sigma_{0.05}$ are available.

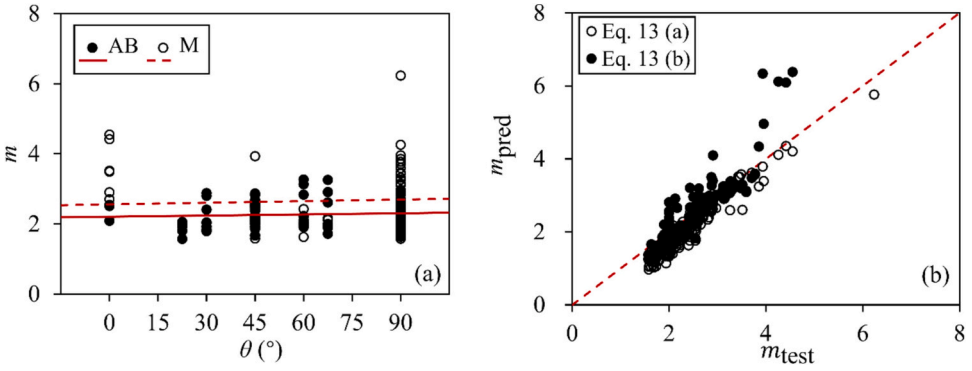

Fig. 25. (a) Distribution of the second strain hardening exponent m at different angles, and (b) evaluation of predictive expressions for m for WAAM steels when measured $\sigma_{1.0}$ (Eq. (13a)), and $\sigma_{2.0}$ (Eq. (13b)) are available.

curves using the basic Ramberg-Osgood model [29,30], as given by Eq. (6). Fig. 24(a) shows that the values of n were scattered, ranging from 0 to 30. It can be attributed to the wide range of feedstock wires, post-treatments, surface conditions, deposition strategies, coupon extraction angles, and material thicknesses employed in the WAAM processes. The values of n have little variation across different surface conditions, but decrease as the coupon extraction angle θ increases.

As noted in Section 2.1.2, the strain hardening exponent n can be calculated by imposing the curve to pass through the 0.2 % proof stress and an additional proof stress. The predictive expression with the additional proof stress of 0.04 % proof stress $f_{0.04}$ (Eq. (42)) was proposed for WAAM steels. Assessment of the expressions is presented in Fig. 24(b), where the predicted values n_{pred} obtained by Eqs. (9), (28), and (42) with different additional proof stresses are plotted against the test values n_{test}.

$$n = \frac{ln(5)}{ln\left(\frac{f_y}{f_{0.04}}\right)} \tag{42}$$

Key statistical values of the strain hardening exponent n are presented in Table 7. It can be seen that Eq. (42) provides more accurate predictions for WAAM steels. It means the 0.04 % proof stress $f_{0.04}$ should be routinely measured and reported by researchers in future experimental programs.

Aside from providing a predictive expression for n, it is also desirable to have representative values for n that capture the general degree of roundedness of the first stage of the stress-strain curve for WAAM steels when the 0.04 % proof stress $f_{0.04}$ is not available. The recommended values, taken as the average of the collated n_{test} values, are provided in Table 8, with a mean value of 15.0 for both machined and as-built coupons.

4.6.2. Strain hardening exponent m

Similar to the test values of n, the second strain hardening exponent m can be obtained by fitting the experimental stress-strain curves using the second-stage Ramberg-Osgood model (Eq. 10). Fig. 25(a) shows that m ranges from 0 to 8. The test values of m for as-built coupons are relatively stable, whereas those for machined coupons are more scattered, resulting in a higher mean m for machined coupons. On the other hand, the test values of m are not significantly affected by coupon extraction angles θ.

Table 9
Statistical results of m_{pred}/m_{test} using different predictive expressions.

	Eq. (13a)	Eq. (13b)	Eq. (42)
Mean	0.855	0.970	1.005
COV	0.136	0.155	0.245

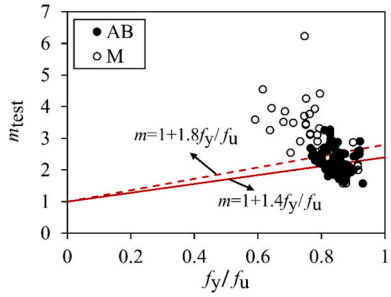

Fig. 26. Assessment of predictive expression for the second strain hardening exponent m for WAAM steels when measured ratios of f_y/f_u are available.

The value of m can be also determined by imposing the second stage of the stress-strain curve to pass through a defined intermediate point, such as 1.0 % proof stress $f_{1.0}$ (Eq. (13a)) and 2.0 % proof stresses $f_{2.0}$ (Eq. (13b)).

Assessment of these two expressions is presented in Fig. 25(b), where the predicted values m_{pred} are plotted against the test values m_{test} using Eqs. (13a) and (13b). The mean and COV of the predicted-to-test result m_{pred}/m_{test} of Eqs. (13a) and (13b) are presented in Table 9. It can be seen that Eq. (13b) yield a satisfying prediction for WAAM steels.

When measured stress-strain data are not available, it is also desirable to have a predictive expression and representative values for m. Eq. (14), expressed in terms of the ratio of yield strength to ultimate strength f_y/f_u, is provided for m of conventional produced steels. Observing a similar trend in the WAAM steel data herein, Eq. (43) was established:

$$m = 1 + 1.4\frac{f_y}{f_u} \text{ for as} - \text{built WAAM steel} \tag{43a}$$

$$m = 1 + 1.8\frac{f_y}{f_u} \text{ for machined WAAM steel} \tag{43b}$$

The test data m_{test} are plotted against the corresponding f_y/f_u ratios for both machined and as-built coupons in Fig. 26, where the predictive expressions are also exhibited. The mean and COV of the predicted-to-test result m_{pred}/m_{test} of Eq. (43) are presented in Table 9. The predictive expression Eq. (43) employs smaller slope values of k, compared to those used for conventional produced steels, such as 2.8 [35], 3.3 [36], and 3.5 [32]. This results in a mean predicted-to-test ratio very close to 1, with a COV of 0.245. Moreover, the required input parameters in Eq. (43) are easier to obtain compared to those in Eq. (13b). As a result, Eq. (43) is more recommended. In instances where the measured f_u is unavailable, it is recommended to adopt the average values m_{test} of 2.5 for both machined and as-built coupons, as given in Table 8.

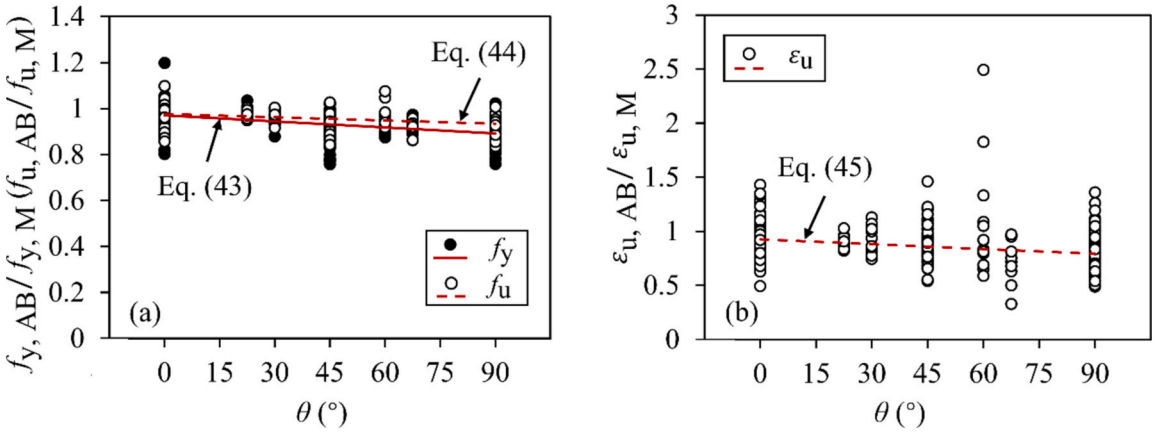

Fig. 27. Comparison of yield and ultimate strength between as-built and machined coupons.

Table 10
Characteristic strength values of ER70S-6 and ER110S-1.

		Machined					As-built				
	θ (°)	Quantity	Average value (MPa)		Characteristic value (MPa)		Quantity	Average value (MPa)		Characteristic value (MPa)	
			$f_{y,a}$	$f_{u,a}$	$f_{y,k}$	$f_{u,k}$		$f_{y,a}$	$f_{u,a}$	$f_{y,k}$	$f_{u,k}$
ER70S-6	All	162	334	451	273	394	225	357	480	296	417
	0	48	356	469	293	411	76	361	489	301	421
	45	43	329	445	275	397	42	352	466	307	416
	90	59	323	443	271	393	95	357	483	288	417
ER110S-1	All	67	623	714	537	644	42	669	774	596	695
	0	13	665	728	593	674	11	690	789	609	704
	45	13	620	716	552	660	9	646	745	596	696
	90	15	594	697	535	642	10	664	788	590	688

4.7. Influence of surface condition

The effects of surface undulations on the strengths (f_y and f_u) and ultimate strain of WAAM carbon steels have been investigated using a corresponding dataset [12,22–24,65,68,85,86,88,90,100]. The ratios of material parameters between as-built and machined coupons, $f_{y,AB}/f_{y,M}$, $f_{u,AB}/f_{u,M}$, and $\varepsilon_{u,AB}/\varepsilon_{u,M}$, are plotted against the coupon extraction angle θ, along with their linear regression lines in Fig. 27, as expressed by Eqs. (44–46). The material parameters show a declining trend as θ increases, which is attributed to greater geometric variability. The ultimate strain experiences a more substantial reduction compared to the strengths (f_y and f_u), with as-built coupons at $\theta = 90°$ exhibiting decreases of 17.3 %, 10.6 %, and 7.3 %, respectively, when compared to equivalent machined coupons. Eqs. (44–46) capture the relationship between the strengths and stain of as-built and machined WAAM steels, highlighting the geometric variability inherent in current WAAM processes.

$$f_{y,AB}/f_{y,M} = 0.97 - 0.05\theta/\pi \ (\theta \text{ in rad}) \quad (44)$$

$$f_{u,AB}/f_{u,M} = 0.98 - 0.03\theta/\pi \ (\theta \text{ in rad}) \quad (45)$$

$$\varepsilon_{u,AB}/\varepsilon_{u,M} = 0.93 - 0.09\theta/\pi \ (\theta \text{ in rad}) \quad (46)$$

4.8. Characteristic strength value

Table 10 summarizes the average and characteristic strength values of WAAM coupons manufactured using different feedstock wires, specifically the low-grade ER70S-6 and the high-grade ER110S-1, which have relatively large quantities in the assembled database. The characteristic values of the yield strength $f_{y,\,k}$ and ultimate strength $f_{u,\,k}$ are defined as the 95 % fractile value, according to EN 1990 [101], which are important and will serve as the basis for determining the design strength values in future research.

Table 11
Measured material properties of WAAM steel coupons used for comparison with predicted stress-strain curves using model exhibiting discontinuous yielding.

Curve	Surface condition	Feedstock wire	t_{nom} (mm)	θ (°)	E (MPa)	f_y (MPa)	f_u (MPa)	ε_u	Source
1	M	ER70S-6	4	0	198,428	320	442	0.16	Laghi et al. [13]
2		ER70S-6	8	30	206,897	315	430	0.21	Huang et al. [12]
3		ER70S-6	8	45	203,882	353	467	0.15	Song et al. [85]
4		3Dprint AM35	12	90	231,602	449	346	0.17	Karabulut et al. [66]
5	AB	ER110S-G	8	0	203,748	604	684	0.10	Weber et al. [90]
6		ER70S-6	3	45	149,276	364	475	0.13	Guo et al. [63]
7		ER70S-6	8	60	215,599	283	409	0.14	Huang et al. [12]
8		ER70S-6	3	90	212,197	337	460	0.18	Huang et al. [65]

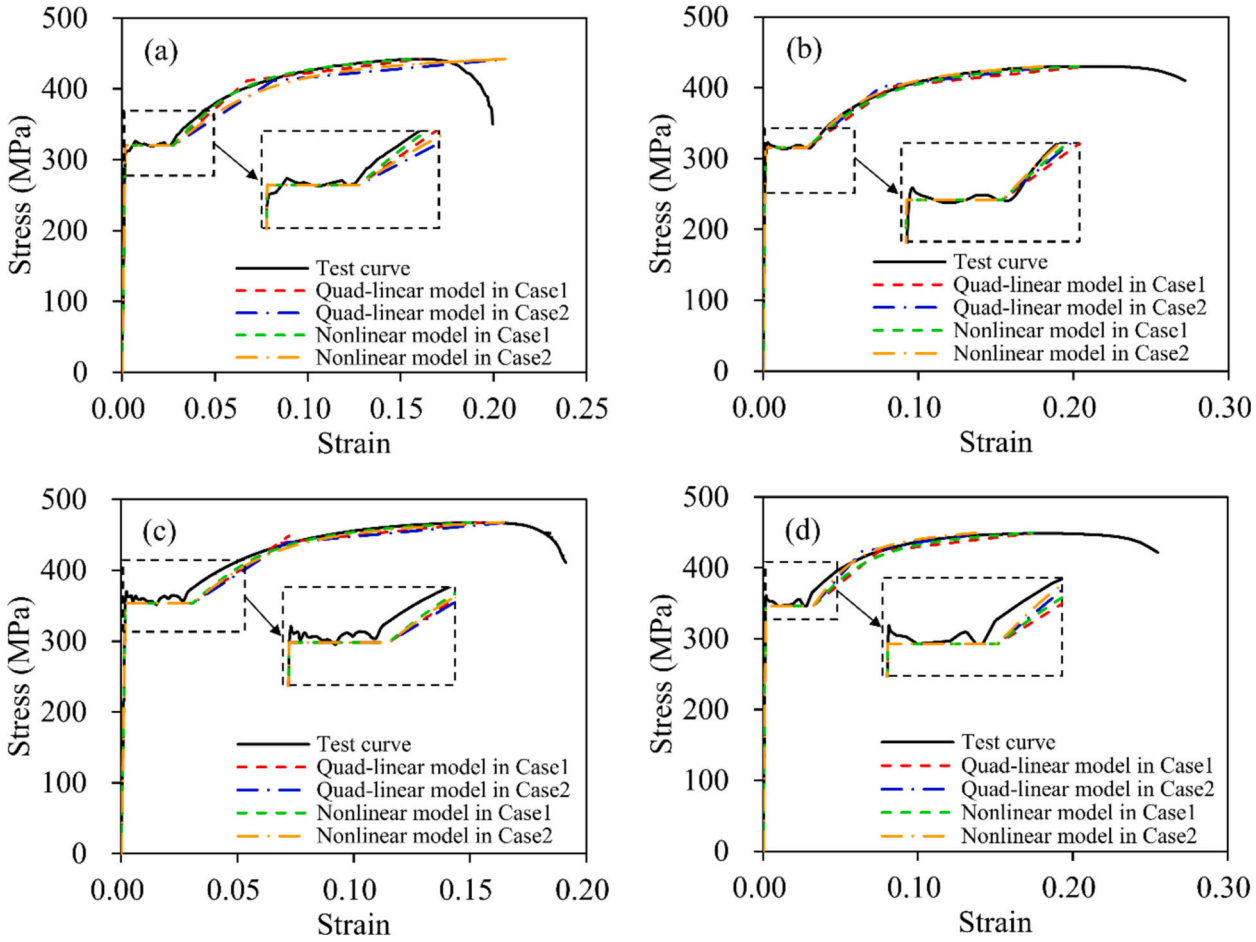

Fig. 28. Comparison of predicted stress-strain curves with test stress-strain curves for machined WAAM steel coupons: (a) Curve 1; (b) Curve 2; (c) Curve 3; and (d) Curve 4.

5. Validation of the stress-strain models

5.1. Comparisons with experimental stress-strain curves

In this section, the accuracy of the proposed quad-linear model and bilinear plus nonlinear hardening model for WAAM steels exhibiting discontinuous yielding, and the two-stage Ramberg-Osgood model for WAAM steels exhibiting continuous yielding is evaluated by comparing sample experimental stress-strain curves (from the collected database) with the corresponding predicted curves. For the validation of the quad-linear and bilinear plus nonlinear hardening model, eight WAAM steel coupons were examined, among which four were machined coupons and four were as-built coupons, with various nominal thicknesses t_{nom}, material strengths and coupon extraction angles θ. The measured geometrical and material properties of these coupons are presented in Table 11. The accuracy of two different predicted curves, which are generated based on: Case (1) the measured material parameters of E, f_y, f_u and ε_u, as reported in Table 11; Case (2) the measured material parameters of E, f_y and f_u, and the predicted values of ε_u using Eq. (35), are assessed. The comparisons between the experimental stress-strain curves and the corresponding predicted curves from both the proposed quad-linear and nonlinear models for the machined and as-built coupons are shown in Figs. 28 and 29 respectively, where good agreements can be seen between the test and predicted stress-strain curves using the proposed models. The degree of agreement in predicting the ultimate strain ε_u significantly effects the model's accuracy, with Case 1 in Fig. 28 (a) being much more accurate than Case 2. Therefore, it is recommended to pay close attention to recording the ultimate strain ε_u during experiments.

For the validation of the two-stage Ramberg-Osgood model, representative comparisons between six test stress-strain curves and the corresponding predicted curves are presented in Figs. 30 and 31, including three for machined coupons and three for as-built coupons, respectively. The accuracy of three different predicted curves, which are generated based on: Case (1) the measured material parameters of E, f_y, f_u, ε_u, n and m, as reported in Table 12; Case (2) the measured material parameters of E, f_y, f_u, and ε_u, the predicted value of n using Eq. (42), and the predicted value of m using Eq. (43); Case (3) the measured material parameters of E, f_y, and f_u, the predicted value of n using Eq. (42), and the predicted value of m using Eq. (43), and the predicted values of ε_u using Eq. (35); Case (4) the measured value of only f_y, the average values of E (202 GPa for WAAM as-built coupons and 192 GPa for WAAM machined coupons), the recommended value of n and m as given in Table 8, and the predicted values of f_u and ε_u obtained from Eqs. (32) and (35) respectively, are examined in this section. The comparisons show that the proposed two-stage Ramberg-Osgood model generally provides an accurate prediction for WAAM steel stress-strain curves. In addition, it was found that although the range of n and m values is relatively large in different cases, as shown in Table 13, it does not have a significant impact on the degree of agreement between the predicted and experimental curves. Meanwhile, the prediction deviation of ultimate strain ε_u will have a significant impact on the final prediction result. In summary, it is recommended to utilise E, f_y, f_u, and ε_u as the basic material parameters that need be recorded in the experiment as the basis for further research such as modelling and finite element research in the future.

5.2. Summary of proposals

The selection of the proposed stress-strain models for WAAM steels, quad-linear, bilinear plus nonlinear hardening, and two-stage Ramberg-Osgood, is based on the yield strength f_y, coupon extraction angle θ, and surface conditions. For specimens with a yield strength f_y below 500 MPa, the stress-strain curves typically show a discontinuous yielding response, making the quad-linear or bilinear plus nonlinear hardening models suitable. Specifically, machined specimens and as-built specimens with $\theta = 0^\circ$ tend to exhibit a flat yield plateau, which is best modelled by the following:

$$f(\varepsilon) = \begin{cases} E\varepsilon & \text{for } \varepsilon \le \varepsilon_y \\ f_y & \text{for } \varepsilon_y < \varepsilon \le \varepsilon_{sh} \\ f_y + E_{sh}(\varepsilon - \varepsilon_{sh}) & \text{for } \varepsilon_{sh} < \varepsilon \le C_1\varepsilon_u \\ f_{C_1\varepsilon_u} + \dfrac{f_u - f_{C_1\varepsilon_u}}{\varepsilon_u - C_1\varepsilon_u}(\varepsilon - C_1\varepsilon_u) & \text{for } C_1\varepsilon_u < \varepsilon \le \varepsilon_u \end{cases} \tag{30a}$$

$$f(\varepsilon) = \begin{cases} E\varepsilon & \text{for } \varepsilon \le \varepsilon_y \\ f_y & \text{for } \varepsilon_y < \varepsilon \le \varepsilon_{sh} \\ f_y + \left(f_u - f_y\right) \times \left\{ K_1\left(\dfrac{\varepsilon - \varepsilon_{sh}}{\varepsilon_u - \varepsilon_{sh}}\right) + K_2\left(\dfrac{\varepsilon - \varepsilon_{sh}}{\varepsilon_u - \varepsilon_{sh}}\right) \Big/ \left[1 + K_3\left(\dfrac{\varepsilon - \varepsilon_{sh}}{\varepsilon_u - \varepsilon_{sh}}\right)^{K_4}\right]^{\frac{1}{K_4}} \right\} & \text{for } \varepsilon_{sh} < \varepsilon \le \varepsilon_u \end{cases} \tag{31a}$$

As-built specimens with $\theta \neq 0^\circ$ often exhibit an inclined yield plateau. These specimens are better modelled using the following models.

$$f(\varepsilon) = \begin{cases} E\varepsilon & \text{for } \varepsilon \le \varepsilon_y \\ f_y + E_p\left(\varepsilon - \varepsilon_y\right) & \text{for } \varepsilon_y < \varepsilon \le \varepsilon_{sh} \\ f_{sh} + E_{sh}(\varepsilon - \varepsilon_{sh}) & \text{for } \varepsilon_{sh} < \varepsilon \le C_1\varepsilon_u \\ f_{C_1\varepsilon_u} + \dfrac{f_u - f_{C_1\varepsilon_u}}{\varepsilon_u - C_1\varepsilon_u}(\varepsilon - C_1\varepsilon_u) & \text{for } C_1\varepsilon_u < \varepsilon \le \varepsilon_u \end{cases} \tag{30b}$$

$$f(\varepsilon) = \begin{cases} E\varepsilon & \text{for } \varepsilon \le \varepsilon_y \\ f_y + E_p\left(\varepsilon - \varepsilon_y\right) & \text{for } \varepsilon_y < \varepsilon \le \varepsilon_{sh} \\ f_{sh} + (f_u - f_{sh}) \times \left\{ K_1\left(\dfrac{\varepsilon - \varepsilon_{sh}}{\varepsilon_u - \varepsilon_{sh}}\right) + K_2\left(\dfrac{\varepsilon - \varepsilon_{sh}}{\varepsilon_u - \varepsilon_{sh}}\right) \Big/ \left[1 + K_3\left(\dfrac{\varepsilon - \varepsilon_{sh}}{\varepsilon_u - \varepsilon_{sh}}\right)^{K_4}\right]^{\frac{1}{K_4}} \right\} & \text{for } \varepsilon_{sh} < \varepsilon \le \varepsilon_u \end{cases} \tag{31b}$$

The material parameters in the models can be calculated using the following predictive expression:

$$\frac{f_u}{f_y} = 1 + \left(\frac{90}{f_y}\right)^{0.8} \tag{34}$$

$$\varepsilon_u = \begin{cases} \left(0.75 - \dfrac{0.3\theta}{\pi}\right)\left(1 - \dfrac{f_y}{f_u}\right) & \text{for machined WAAM steels } (\theta \text{ in rad}) \\ \left(0.70 - \dfrac{0.5\theta}{\pi}\right)\left(1 - \dfrac{f_y}{f_u}\right) & \text{for machined WAAM steels } (\theta \text{ in rad}) \end{cases} \tag{35a}$$

$$\varepsilon_{sh} = \begin{cases} 0.1\dfrac{f_y}{f_u} - 0.045 & \text{for } 0.015 \le \varepsilon_{sh} \le 0.03 \text{ for machined WAAM steels} \\ 0.1\dfrac{f_y}{f_u} - 0.051 & \text{for } 0.015 \le \varepsilon_{sh} \le 0.03 \text{ for as-built WAAMsteels} \end{cases} \tag{37a}$$

$$E_p = \begin{cases} 0 & \text{for flat yield plateau} \\ 0.007E & \text{for inclined yield plateau} \end{cases} \tag{39a}$$

$$C_1 = \frac{\varepsilon_{sh} + 0.3(\varepsilon_u - \varepsilon_{sh})}{\varepsilon_u} \tag{40}$$

$$E_{sh} = \begin{cases} \dfrac{f_u - f_y}{0.4(\varepsilon_u - \varepsilon_{sh})} & \text{for flat yield plateau} \\ \dfrac{f_u - f_y}{0.5(\varepsilon_u - \varepsilon_{sh})} & \text{for inclined yield plateau} \end{cases} \tag{41a}$$

For WAAM specimens with a yield strength above 500 MPa, the two-stage Ramberg-Osgood model and its predictive expressions of material parameters are preferred:

$$\varepsilon = \begin{cases} \dfrac{f}{E} + 0.002\left(\dfrac{f}{f_y}\right)^n & \text{for } f \le f_y \\ \dfrac{f - f_y}{E_{0.2}} + \left(\varepsilon_u - \varepsilon_{0.2} - \dfrac{f_u - f_y}{E_{0.2}}\right)\left(\dfrac{f - f_y}{f_u - f_y}\right)^m + \varepsilon_{0.2} & \text{for } f_y < f \le f_u \end{cases} \tag{10}$$

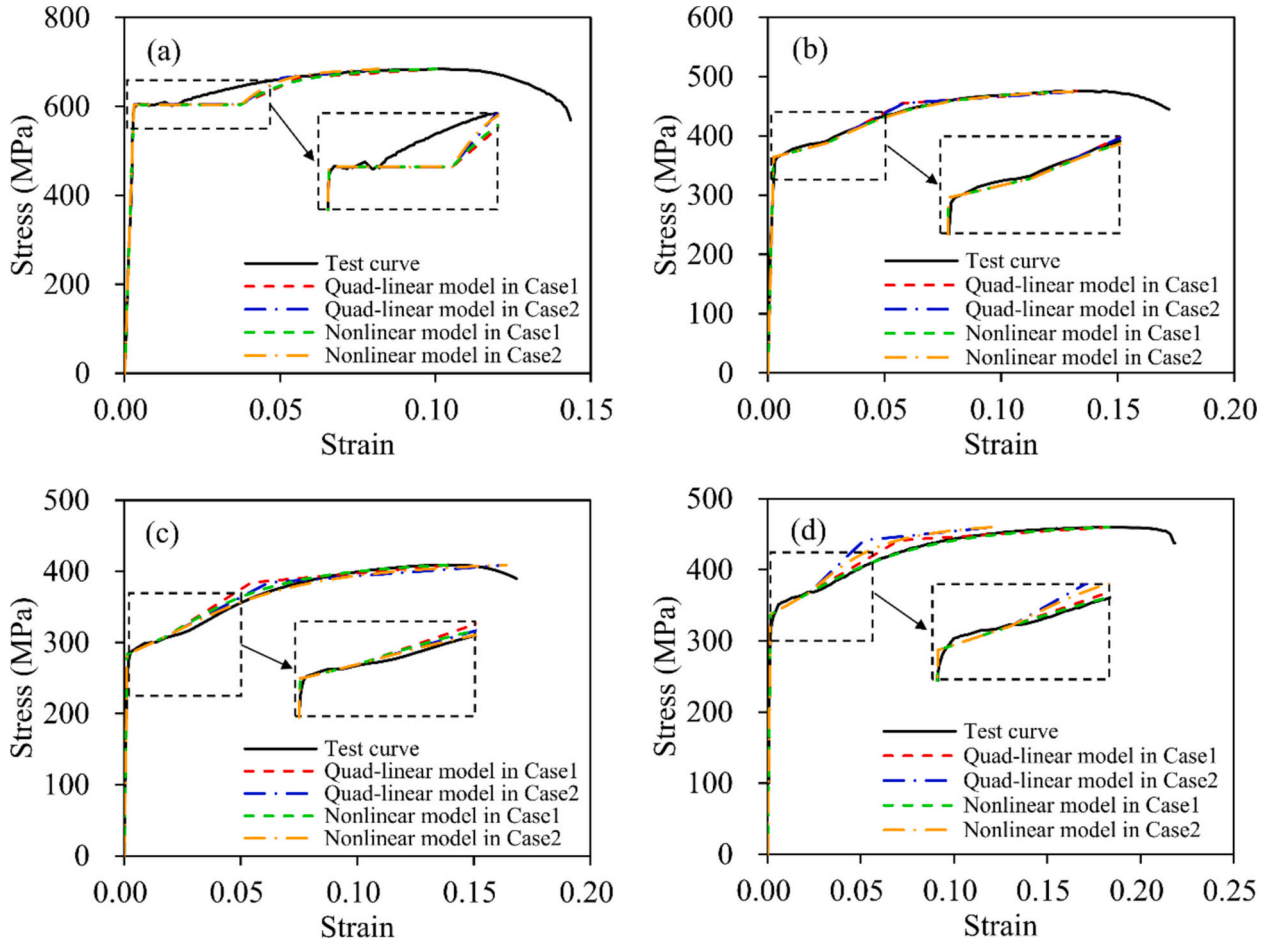

Fig. 29. Comparison of predicted stress-strain curves using model exhibiting discontinuous yielding with test stress-strain curves for as-built WAAM steel coupons: (a) Curve 5; (b) Curve 6; (c) Curve 7; and (d) Curve 8.

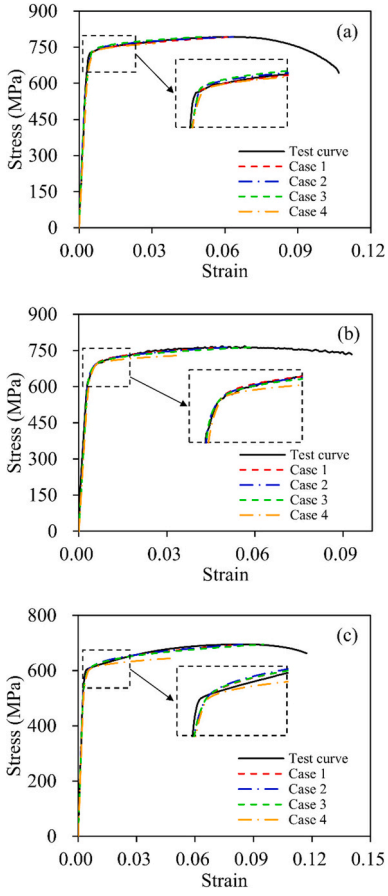

Fig. 30. Comparison of predicted stress-strain curves using model exhibiting continuous yielding with test stress-strain curves for machined WAAM steel coupons: (a) Curve 9; (b) Curve 10; and (c) Curve 11.

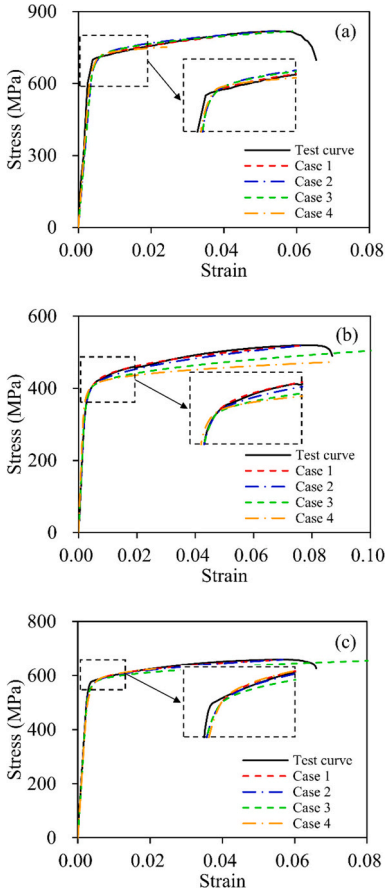

Fig. 31. Comparison of predicted stress-strain curves using model exhibiting continuous yielding with test stress-strain curves for as-built WAAM steel coupons: (a) Curve 12; (b) Curve 13; and (c) Curve 14.

$$n = \frac{ln(5)}{ln\left(\frac{f_y}{f_{0.04}}\right)} \tag{42}$$

$$m = \begin{cases} 1 + 1.4\dfrac{f_y}{f_u} & \text{for as} - \text{built WAAM steel} \\ 1 + 1.8\dfrac{f_y}{f_u} & \text{for machined WAAM steel} \end{cases} \tag{43a}$$

6. Conclusions

An investigation into the constitutive modelling of WAAM carbon steel is presented in this paper. A thorough investigation into the constitutive modelling of WAAM carbon steel, based on over 700 tensile tests covering various feedstock wires, post-treatments, surface conditions, deposition strategies, coupon extraction angles, and material thicknesses, has been conducted. The following conclusions are drawn from the research:

1) The quad-linear and bilinear plus nonlinear hardening models, originally designed for hot-rolled steels, were adapted to capture the flat or inclined yield plateau and strain hardening behaviour of WAAM steels with yield strength f_y below 500 MPa.
2) For WAAM steels with yield strength f_y above 500 MPa, the two-stage Ramberg-Osgood model, developed for stainless and cold-formed steels, was proposed to describe the rounded stress-strain response.
3) Predictive expressions and recommended values for material parameters were established from a comprehensive review of experimental data, which included various feedstock wires, post-treatments, surface conditions, deposition techniques, coupon extraction angles, and material thicknesses.
4) The models, based on four recommended key material properties (E, f_y, f_u, and ε_u), effectively represent the complete stress-strain curves of WAAM steels. These models are suitable for analytical modelling, numerical simulations, and advanced design of WAAM steel structures.
5) The criteria for yielding response remain insufficiently defined, and the effects of various factors on material parameters, such as f_u, are not yet fully understood. Future research will aim to address these limitations by incorporating a larger dataset, conducting additional experiments, and exploring a broader range of factors.

CRediT authorship contribution statement

Yunyi Liu: Writing – original draft, Validation, Methodology, Investigation. **Jun Ye:** Writing – review & editing, Supervision,

Table 12
Measured material properties of WAAM steel coupons used for comparison with predicted stress-strain curves using model exhibiting continuous yielding.

Curve	Surface condition	Feedstock wire	t_{nom} (mm)	θ (°)	E (MPa)	f_y (MPa)	f_u (MPa)	ε_u	n	m	Source
9	M	ER110S-G	3	90	238,690	726	793	0.06	7.1	2.0	Weber et al. [90]
10		ER90S-B91	6.5	90	206,491	687	764	0.05	22.0	2.9	Li et al. [16]
11		ER110S-G	8	45	206,749	597	695	0.08	16.1	2.4	Huang et al. [12]
12	AB	ER120S-G	6.5	90	177,064	711	818	0.05	23.6	1.6	Chen et al. [14]
13		ER50–6	3.6	45	163,836	401	519	0.08	11.3	2.6	Liu et al. [22]
14		ER110S-G	3	0	206,167	575	659	0.06	20.8	2.5	Huang et al. [12]

Table 13
The n and m values in different cases.

	n			m		
Curve	Case1	Case2/3	Case 4	Case1	Case2/3	Case 4
9	7.1	6.8	15.0	2.0	2.6	2.5
10	22.0	23.3	15.0	2.9	2.6	2.5
11	16.1	16.7	15.0	2.4	2.5	2.5
12	23.6	22.0	15.0	1.6	2.2	2.5
13	11.3	11.5	15.0	2.6	2.1	2.5
14	20.8	20.8	15.0	2.5	2.2	2.5

Resources, Project administration, Investigation, Funding acquisition, Conceptualization. **Xi Guo:** Writing – review & editing, Supervision, Investigation. **Guan Quan:** Writing – review & editing, Supervision, Project administration, Conceptualization. **Zhen Wang:** Writing – review & editing, Resources, Investigation. **Yang Zhao:** Writing – review & editing, Supervision, Resources, Project administration, Funding acquisition.

Declaration of competing interest

The authors declare that they have no known competing financial interests or personal relationships that could have appeared to influence the work reported in this paper.

Data availability

The data presented in this work will be made available upon reasonable request.

Acknowledgement

The authors would like to acknowledge the financial support to this project by the National Natural Science Foundation of China (No. 52208215) and the Natural Science Foundation of Zhejiang Province (No. LQ22E080008).

References

[1] S.I. Evans, J. Wang, J. Qin, Y. He, P. Shepherd, J. Ding, A review of WAAM for steel construction – manufacturing, material and geometric properties, design, and future directions, Structures 44 (2022) 1506–1522.
[2] L. Gardner, Metal additive manufacturing in structural engineering – review, advances, opportunities and outlook, Structures 47 (2023) 2178–2193.
[3] L. Gardner, P. Kyvelou, G. Herbert, C. Buchanan, Testing and initial verification of the world's first metal 3D printed bridge, J. Constr. Steel Res. 172 (2020) 106233.
[4] J. Ye, P. Kyvelou, F. Gilardi, H. Lu, M. Gilbert, L. Gardner, An end-to-end framework for the additive manufacture of optimized tubular structures, IEEE Access 9 (2021) 165476–165489.
[5] P. Kyvelou, A. Spinasa, L. Gardner, Testing and analysis of optimized wire arc additively manufactured steel trusses, J. Struct. Eng. 150 (2024) 04024008.
[6] T. Feucht, J. Lange, M. Erven, 3-D-printing with steel: additive manufacturing of connection elements and beam reinforcements, CE Papers 3 (2019) 343–348.
[7] T. Feucht, B. Waldschmitt, J. Lange, M. Erven, 3D-printing with steel: additive manufacturing of a bridge in situ, CE Papers 4 (2021) 1695–1701.
[8] N. Hadjipantelis, B. Weber, C. Buchanan, L. Gardner, Description of anisotropic material response of wire and arc additively manufactured thin-walled stainless steel elements, Thin-Walled Struct. 171 (2022) 108634.
[9] P. Kyvelou, H. Slack, D. Daskalaki Mountanou, M.A. Wadee, T.B. Britton, C. Buchanan, et al., Mechanical and microstructural testing of wire and arc additively manufactured sheet material, Mater. Des. 192 (2020) 108675.
[10] M.-T. Chen, Z. Gong, T. Zhang, W. Zuo, Y. Zhao, O. Zhao, et al., Mechanical behavior of austenitic stainless steels produced by wire arc additive manufacturing, Thin-Walled Struct. 196 (2024) 111455.
[11] M.-T. Chen, Y. Chen, W. Zuo, X. Yun, O. Zhao, S.-W. Liu, et al., Experimental investigation on the tensile behavior of wire arc additively manufactured duplex stainless steel plates, Eng. Struct. 321 (2024) 118764.
[12] C. Huang, P. Kyvelou, R. Zhang, T. Ben Britton, L. Gardner, Mechanical testing and microstructural analysis of wire arc additively manufactured steels, Mater. Des. 216 (2022) 110544.
[13] V. Laghi, L. Arrè, L. Tonelli, G. Di Egidio, L. Ceschini, I. Monzón, et al., Mechanical and microstructural features of wire-and-arc additively manufactured carbon steel thick plates, Int. J. Adv. Manuf. Technol. 127 (2023) 1391–1405.
[14] M.-T. Chen, T. Zhang, Z. Gong, W. Zuo, Z. Wang, L. Zong, et al., Mechanical properties and microstructure characteristics of wire arc additively manufactured high-strength steels, Eng. Struct. 300 (2024) 117092.
[15] P. Dirisu, S. Ganguly, A. Mehmanparast, F. Martina, S. Williams, Analysis of fracture toughness properties of wire + arc additive manufactured high strength low alloy structural steel components, Mater. Sci. Eng. A 765 (2019) 138285.
[16] K. Li, M.A. Klecka, S. Chen, W. Xiong, Wire-arc additive manufacturing and post-heat treatment optimization on microstructure and mechanical properties of grade 91 steel, Addit. Manuf. 37 (2021) 101734.
[17] J. Müller, M. Grabowski, C. Müller, J. Hensel, J. Unglaub, K. Thiele, et al., Design and parameter identification of wire and arc additively manufactured (WAAM) steel bars for use in construction, Metals 9 (2019) 725.
[18] A. Vahedi Nemani, M. Ghaffari, A. Nasiri, Comparison of microstructural characteristics and mechanical properties of shipbuilding steel plates fabricated by conventional rolling versus wire arc additive manufacturing, Addit. Manuf. 32 (2020) 101086.
[19] C. Huang, X. Meng, C. Buchanan, L. Gardner, Flexural buckling of wire arc additively manufactured tubular columns, J. Struct. Eng. 148 (2022) 04022139.
[20] P. Kyvelou, C. Huang, L. Gardner, C. Buchanan, Structural testing and design of wire arc additively manufactured square hollow sections, J. Struct. Eng. 147 (2021) 04021218.
[21] V. Laghi, M. Palermo, G. Gasparini, V.A. Girelli, T. Trombetti, Experimental results for structural design of wire-and-arc additive manufactured stainless steel members, J. Constr. Steel Res. 167 (2020) 105858.
[22] Y. Liu, J. Ye, Y. Yang, G. Quan, Z. Wang, W. Zhao, et al., Experimental study on wire and arc additively manufactured steel double-shear bolted connections, J. Build. Eng. 76 (2023) 107330.
[23] Y. Liu, J. Ye, H. Lu, G. Quan, Z. Wang, Y. Zhao, et al., Structural behaviour and design of wire arc additively manufactured bolted connections with thick plates, Structures 70 (2024) 107573.
[24] J. Ye, Y. Liu, Y. Yang, Z. Wang, O. Zhao, Y. Zhao, Testing, analysis and design of wire and arc additively manufactured steel bolted connections, Eng. Struct. 296 (2023) 116939.
[25] W. Zuo, M.-T. Chen, O. Zhao, A. Su, S.-W. Liu, F. Xu, et al., Behavior of wire arc additively manufactured 316L austenitic stainless steel single shear bolted connections, Thin-Walled Struct. 202 (2024) 112075.
[26] W. Zuo, M.-T. Chen, S.-W. Liu, X. Yun, O. Zhao, Y. Huang, et al., Experimental investigation on double-lap shear behavior of 3D printed austenitic stainless steel bolted connections, Eng. Struct. 317 (2024) 118501.
[27] W. Zuo, M.-T. Chen, O. Zhao, A. Su, S.-W. Liu, X. Yun, et al., Structural performance of wire arc additively manufactured duplex stainless steel single-lap shear bolted connections, Eng. Struct. 319 (2024) 118706.
[28] X. Yun, L. Gardner, Stress-strain curves for hot-rolled steels, J. Constr. Steel Res. 133 (2017) 36–46.
[29] W. Ramberg, W.R. Osgood, Description of Stress-Strain Curves by Three Parameters. Technical Note No. 902, National Advisory Committee for Aeronautics, Washington (DC), 1943.
[30] H. Hill, Determination of Stress-Strain Relations from" Offset" Yield Strength Values. Technical Note No. 927, National Advisory Committee for Aeronautics, Washington (DC), 1944.

[31] E. Mirambell, E. Real, On the calculation of deflections in structural stainless steel beams: an experimental and numerical investigation, J. Constr. Steel Res. 54 (2000) 109–133.
[32] JR RK, Full-range stress–strain curves for stainless steel alloys, J. Constr. Steel Res. 59 (2003) 47–61.
[33] W.M. Quach, J.G. Teng, K.F. Chung, Three-stage full-range stress-strain model for stainless steels, J. Struct. Eng. 134 (2008) 1518–1527.
[34] P. Hradil, A. Talja, E. Real, E. Mirambell, B. Rossi, Generalized multistage mechanical model for nonlinear metallic materials, Thin-Walled Struct. 63 (2013) 63–69.
[35] I. Arrayago, E. Real, L. Gardner, Description of stress–strain curves for stainless steel alloys, Mater. Des. 87 (2015) 540–552.
[36] L. Gardner, X. Yun, Description of stress-strain curves for cold-formed steels, Constr. Build. Mater. 189 (2018) 527–538.
[37] G. Shi, X. Zhu, H. Ban, Material properties and partial factors for resistance of high-strength steels in China, J. Constr. Steel Res. 121 (2016) 65–79.
[38] X.-Q. Wang, Z. Tao, U. Katwal, C. Hou, Tensile stress-strain models for high strength steels, J. Constr. Steel Res. 186 (2021) 106879.
[39] C. Huang, P. Kyvelou, L. Gardner, Stress-strain curves for wire arc additively manufactured steels, Eng. Struct. 279 (2023) 115628.
[40] EN ISO 6892-1, Metallic Materials - Tensile Testing - Part 1: Method of Test at Room Temperature, European Committee for Standardisation, Brussels, 2019.
[41] A.J. Sadowski, J.M. Rotter, T. Reinke, T. Ummenhofer, Statistical analysis of the material properties of selected structural carbon steels, Struct. Saf. 53 (2015) 26–35.
[42] W.M. Quach, J.F. Huang, Stress-strain models for light gauge steels, Procedia Eng. 14 (2011) 288–296.
[43] EN 1993-1-4, Eurocode 3: Design of Steel Structures — Part 1–4: General Rules — Supplementary Rules for Stainless Steels, European Committee for Standardization, Brussels, 2006.
[44] K. Rasmussen, G. Hancock, Design of cold-formed stainless steel tubular members. II: Beams, J. Struct. Eng. 119 (1993) 2368–2386.
[45] L. Gardner, D.A. Nethercot, Experiments on stainless steel hollow sections—Part 1: material and cross-sectional behaviour, J. Constr. Steel Res. 60 (2004) 1291–1318.
[46] Y. Fukumoto, New constructional steels and structural stability, Eng. Struct. 18 (1996) 786–791.
[47] GB/T 8110–2020, Wire Electrodes and Weld Deposits for Gas Shielded Metal Arc Welding of Non-alloy and Fine Grain Steels, Standardization of Administration of the People's Republic of China, Beijing, 2020.
[48] AWS A518/A518M, Specification for Carbon Steel Electrodes and Rods for Gas Shielded Arc Welding, American Welding Society, 2021.
[49] AWS A528/A528M, Specification for Carbon Steel Electrodes and Rods for Gas Shielded Arc Welding, American Welding Society, 2020.
[50] EN ISO 14341, Welding Consumables—Wire Electrodes and Weld Deposits for Gas Shielded Metal Arc Welding of Non Alloy and Fine Grain Steels—Classification, European Committee for Standardization, Brussels, 2020.
[51] AFNOR NF A37–-5021984, Cold-rolled Strips for Heat Treatment in Non-alloy Carbon Steels. France, 2024.
[52] GetData Graph Digitizer 2.26 [Software], 2013.
[53] M.R.U. Ahsan, A.N.M. Tanvir, T. Ross, A. Elsawy, M.-S. Oh, D.B. Kim, Fabrication of bimetallic additively manufactured structure (BAMS) of low carbon steel and 316L austenitic stainless steel with wire + arc additive manufacturing, Rapid Prototyp. J. 26 (2019) 519–530.
[54] M.R.U. Ahsan, A.N.M. Tanvir, G.-J. Seo, B. Bates, W. Hawkins, C. Lee, et al., Heat-treatment effects on a bimetallic additively-manufactured structure (BAMS) of the low-carbon steel and austenitic-stainless steel, Addit. Manuf. 32 (2020) 101036.
[55] E. Aldalur, F. Veiga, A. Suárez, J. Bilbao, A. Lamikiz, Analysis of the wall geometry with different strategies for high deposition wire arc additive manufacturing of mild steel, Metals 10 (2020) 892.
[56] Z. Al-Nabulsi, J.T. Mottram, M. Gillie, N. Kourra, M.A. Williams, Mechanical and X ray computed tomography characterisation of a WAAM 3D printed steel plate for structural engineering applications, Constr. Build. Mater. 274 (2021) 121700.
[57] A. Astarita, G. Campatelli, P. Corigliano, G. Epasto, F. Montevecchi, F. Scherillo, et al., Microstructure and mechanical properties of specimens produced using the wire-arc additive manufacturing process, Proc. Inst. Mech. Eng. C J. Mech. Eng. Sci. 235 (2019) 1788–1798.
[58] Y. Ayan, N. Kahraman, Wire arc additive manufacturing of low-carbon mild steel using two different 3D printers, Phys. Met. Metallogr. 122 (2021) 1521–1529.
[59] C. Bourlet, S. Zimmer-Chevret, R. Pesci, R. Bigot, A. Robineau, F. Scandella, Microstructure and mechanical properties of high strength steel deposits obtained by wire-arc additive manufacturing, J. Mater. Process. Technol. 285 (2020) 116759.
[60] A. Ermakova, A. Mehmanparast, S. Ganguly, N. Razavi, F. Berto, Investigation of mechanical and fracture properties of wire and arc additively manufactured low carbon steel components, Theor. Appl. Fract. Mech. 109 (2020) 102685.
[61] Q. Fang, L. Zhao, C.-x. Chen, Y. Cao, L. Song, Y. Peng, et al., 800 MPa class HSLA steel block part fabricated by WAAM for building applications: tensile properties at ambient and elevated (600°C) temperature, Adv. Mater. Sci. Eng. 2022 (2022) 1–13.
[62] M. Ghaffari, A. Vahedi Nemani, M. Rafieazad, A. Nasiri, Effect of solidification defects and HAZ softening on the anisotropic mechanical properties of a wire arc additive-manufactured low-carbon low-alloy steel part, JOM 71 (2019) 4215–4224.
[63] X. Guo, P. Kyvelou, J. Ye, L.H. Teh, L. Gardner, Experimental investigation of wire arc additively manufactured steel single-lap shear bolted connections, Thin-Walled Struct. 181 (2022) 110029.
[64] C. Guo, M. Liu, R. Hu, T. Yang, B. Wei, F. Chen, et al., High-strength wire + arc additive manufactured steel, Int. J. Mater. Res. 111 (2020) 325–331.
[65] C. Huang, L. Li, N. Pichler, E. Ghafoori, L. Susmel, L. Gardner, Fatigue testing and analysis of steel plates manufactured by wire-arc directed energy deposition, Addit. Manuf. 73 (2023) 103696.
[66] B. Karabulut, X. Ruan, S. MacDonald, J. Dobrić, B. Rossi, Fatigue of wire arc additively manufactured components made of unalloyed S355 steel, Int. J. Fatigue 184 (2024) 108317.
[67] Y. Khandelwal, R.K. Gupta, K.K. Verma, A. Mandal, A Study of Microstructure and Mechanical Properties of Wire Arc Additive Manufactured Component with ER70S6 Alloy Wire Using CMT Process, Springer Singapore, Singapore, 2021, pp. 133–146.
[68] G. Kotteman, Steel 3D Printing for Structures: An Explorative Study on the Tear-out Strength of a Pin or Bolt in a Wire and Arc Additively Manufactured Carbon Steel Plate, Delft University of Technology, 2020.
[69] R. Kühne, M. Feldmann, S. Citarelli, U. Reisgen, R. Sharma, L. Oster, 3D printing in steel construction with the automated wire arc additive manufacturing, CE Papers 3 (2019) 577–583.
[70] V. Kumar, A. Mandal, A critical investigation of the anisotropic behavior in the WAAM-fabricated structure, Rapid Prototyp. J. 30 (2024) 1023–1045.
[71] P. Kyvelou, C. Huang, J. Li, L. Gardner, Residual stresses in steel I-sections strengthened by wire arc additive manufacturing, Structures 60 (2024) 105828.
[72] J. Lange, T. Feucht, M. Erven, 3D-printing with steel - additive manufacturing connections and structures, CE Papers 4 (2021) 2–7.
[73] V.T. Le, D.S. Mai, Q.H. Hoang, A study on wire and arc additive manufacturing of low-carbon steel components: process stability, microstructural and mechanical properties, J. Braz. Soc. Mech. Sci. Eng. 42 (2020) 480.
[74] Z. Lin, C. Goulas, W. Ya, M.J.M. Hermans, Microstructure and mechanical properties of medium carbon steel deposits obtained via wire and arc additive manufacturing using metal-cored wire, Metals 9 (2019) 673.
[75] X. Lu, Y.F. Zhou, X.L. Xing, L.Y. Shao, Q.X. Yang, S.Y. Gao, Open-source wire and arc additive manufacturing system: formability, microstructures, and mechanical properties, Int. J. Adv. Manuf. Technol. 93 (2017) 2145–2154.
[76] C. Ma, C. Li, Y. Yan, Y. Liu, X. Wu, D. Li, et al., Investigation of the in-situ gas cooling of carbon steel during wire and arc additive manufacturing, J. Manuf. Process. 67 (2021) 461–477.
[77] D. Michl, B. Sydow, M.J.P.M. Bambach, Ring rolling of pre-forms made by wire-arc additive manufacturing 47 (2020) 342–348.
[78] J. Müller, J. Hensel, K. Dilger, Mechanical properties of wire and arc additively manufactured high-strength steel structures, Weld. World 66 (2021) 395–407.
[79] B.P. Nagasai, S. Malarvizhi, V. Balasubramanian, Mechanical properties of wire arc additive manufactured carbon steel cylindrical component made by gas metal arc welding process, J. Mech. Behav. Mater. 30 (2021) 188–198.
[80] M. Rafieazad, A.V. Nemani, M. Ghaffari, A. Nasiri, On microstructure and mechanical properties of a low-carbon low-alloy steel block fabricated by wire arc additive manufacturing, J. Mater. Eng. Perform. 30 (2021) 4937–4945.
[81] L.P. Raut, R.V. Taiwade, Microstructure and mechanical properties of wire arc additively manufactured bimetallic structure of austenitic stainless steel and low carbon steel, J. Mater. Eng. Perform. 31 (2022) 8531–8541.
[82] T.A. Rodrigues, V.R. Duarte, D. Tomás, J.A. Avila, J.D. Escobar, E. Rossinyol, et al., In-situ strengthening of a high strength low alloy steel during wire and arc additive manufacturing (WAAM), Addit. Manuf. 34 (2020) 101200.
[83] Levy Ron, Leon Dolev, Aghion Shirizly, Environmental behavior of low carbon steel produced by a wire arc additive manufacturing process, Metals 9 (2019) 888.
[84] V.-A. Silvestru, I. Ariza, J. Vienne, L. Michel, A.M. Aguilar Sanchez, U. Angst, et al., Performance under tensile loading of point-by-point wire and arc additively manufactured steel bars for structural components, Mater. Des. 205 (2021) 109740.
[85] S.-S. Song, J. Chen, J. Ye, G. Quan, Z. Wang, J. Xiao, Test and analysis of the interfacial bond behaviour of circular concrete-filled wire-arc additively manufactured steel tubes, J. Build. Eng. 82 (2024) 108171.
[86] S.-S. Song, J. Chen, G. Quan, J. Ye, Y. Zhao, Numerical analysis and design of concrete-filled wire arc additively manufactured steel tube under axial compression, Eng. Struct. 301 (2024) 117294.
[87] L. Sun, F. Jiang, R. Huang, D. Yuan, C. Guo, J. Wang, Microstructure and mechanical properties of low-carbon high-strength steel fabricated by wire and arc additive manufacturing, Metals 10 (2020) 216.
[88] T. Tankova, D. Andrade, R. Branco, C. Zhu, D. Rodrigues, L. Simões da Silva, Characterization of robotized CMT-WAAM carbon steel, J. Constr. Steel Res. 199 (2022) 107624.
[89] U. Tripathi, N. Saini, R.S. Mulik, M.M. Mahapatra, Effect of build direction on the microstructure evolution and their mechanical properties using GTAW based wire arc additive manufacturing, CIRP J. Manuf. Sci. Technol. 37 (2022) 103–109.
[90] B. Weber, X. Meng, R. Zhang, M. Nitawaki, T. Sagawa, L. Gardner, Tensile behaviour of WAAM high strength steel material and members, Mater. Des. 237 (2024) 112517.

[91] G.A. Webster, R. Ribble, K. Chou, A. Krishnamurthy, E. Johnson, S. Zekriardehani, et al., Fatigue characterization of wire arc additive manufactured AWS ER100S-G steel: fully reversed condition, Eng. Fail. Anal. 153 (2023) 107562.
[92] H. Xin, I. Tarus, L. Cheng, M. Veljkovic, N. Persem, L. Lorich, Experiments and numerical simulation of wire and arc additive manufactured steel materials, Structures 34 (2021) 1393–1402.
[93] A.S. Yildiz, K. Davut, B. Koc, O. Yilmaz, Wire arc additive manufacturing of high-strength low alloy steels: study of process parameters and their influence on the bead geometry and mechanical characteristics, Int. J. Adv. Manuf. Technol. 108 (2020) 3391–3404.
[94] A. Haar, Zur theorie der orthogonalen funktionensysteme, Math. Ann. 69 (1910) 331–371.
[95] K L, A method for the solution of certain non-linear problems in least squares, Q. Appl. Math. 2 (1944) 164–168.
[96] D.W. Marquardt, An algorithm for least-squares estimation of nonlinear parameters, J. Soc. Ind. Appl. Math. 11 (1963) 431–441.
[97] EN 1993-1-1, Eurocode 3 - Design of Steel Structures – Part 1–1: General Rules and Rules for Building, European Committee for Standardisation, Brussels, 2020.
[98] AISI S100–16w/S1–-18, North American Specification for the Design of Cold-Formed Steel Structural Members, American Iron and Steel Institue, Washington DC, 2016.
[99] EN 1011–-2:2001, Welding—Recommendations for Welding of Metallic Materials—Part 2: Arc Welding of Ferritic Steels, European Committee for Standardization, Brussels, 2001.
[100] X. Guo, P. Kyvelou, J. Ye, L. Gardner, Experimental investigation of wire arc additively manufactured steel T-stub connections, J. Constr. Steel Res. 211 (2023) 108106.
[101] EN 1990, Eurocode - Basis of Structural Design, European Committee for Standardisation, Brussels, 2002.